Sonar Acoustics

Kathryn Harriman
St. Anne's College
Oxford

Dissertation submitted in partial fulfilment of
the requirements for the degree of Master of Science in
Mathematical Modelling and Numerical Analysis
at Oxford University

September 1997

Acknowledgements

I would like to thank my supervisor Dr D.J. Allwright for his help and guidance during the writing of this dissertation and Dr D. Butler of Thomson Marconi Sonar Systems Ltd for suggesting the problem and providing further useful ideas throughout. I am also grateful to him for his work on the problem, the information about the sonar set and the original programs which have been adapted to produce the results for the mode model. Thanks must also go to Thomson Marconi Sonar Systems Ltd for their financial support, to the Engineering and Physical Sciences Research Council for funding this year of my M.Sc., to Keith Gillow for his invaluable help with LaTeX, and last, but not least, to my parents for their constant support during my time in Oxford.

Abstract

The problem of producing a model to determine the beam pattern produced by a sonar set in the form of a circular cylinder with hemispherical end caps is studied. The beam width and the position of the beam centre are also considered and the results of the models are compared with experimental findings. Possible reasons for the discrepancies between these theoretical and experimental results are examined, providing insight into developing more sophisticated mathematical models. The beam patterns were produced using a combination of Matlab and Fortran 77 programs incorporating subroutines from the NAG library. Experimental results and data are included with the kind permission of Thomson Marconi Sonar Systems Ltd.

Contents

Chapter 1

Introduction

1.1 Sonar

Sound travels relatively easily through water and hence it has been applied in a variety of ways to the exploration and use of the seas. These uses of underwater sound make up the science of sonar, an acronym for **so**und **na**vigation and **r**anging.

The ideas of sonar go back hundreds of years to when people used to place one end of a long tube in water and the other end to their ear in order to hear ships a long way off. Although this idea is rather primitive, it continued to be used until the beginning of this century although it was slightly more sophisticated by then, having a second tube between the other ear and a second point in the sea so that a direction could be found and hence the bearing of the target deduced.

The years of both world wars saw great developments in the understanding and uses of sonar for military purposes. Since then there has also been progress in utilising sonar for non-military reasons, for example in depth sounders, fish finding, divers' aids and position marking to name but a few. However the military uses of underwater sound continue to be an area of considerable interest.

1.2 The Sonar Set

A sonar set can be either active or passive (listening). In the former sound is generated by a transmitter, these sound waves then travel through the sea to the target then they return as sonar echoes to the receiver. The receiver contains hydrophones which convert the sound into electricity, this electric output can then be amplified and processed in order to determine the position of the object. Such an active sonar system is said to *echo-range* on its target. A passive or listening set however simply uses sound radiated by its target so only one-way transmission through the sea occurs.

Here we will be considering an active sonar set which forms an underwater mine searcher. As in figure 1.1 the set is made up of a vertical elastic circular cylinder made of a plastic called ABS [1](believed to be isotropic) which is surrounded internally and externally by sea water. Inside is a curved array of hydrophones which transmits sound and a straight array below it receives sound in order to determine the position of unidentified objects in the sea. The cylinder has steel end caps and in addition to the arrays there is other equipment inside including a mechanism for turning the device about its axis and electronics for processing the array outputs. This may need to be taken into account when formulating a mathematical model of the device.

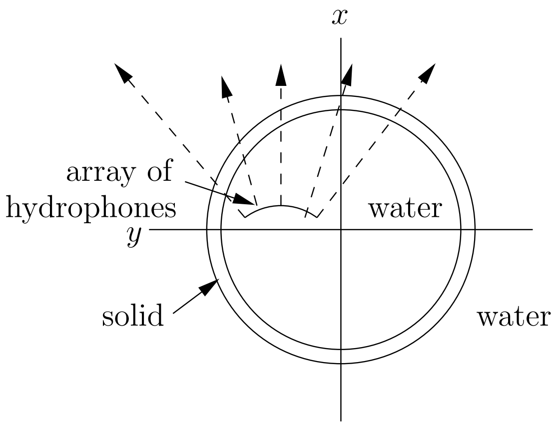

Figure 1.1: Horizontal cross section of a sonar set.

The problem we shall be considering concerns the amplitude profile emitted by the array in such a sonar set. The wavelength used is comparable to the thickness of the cylinder but much less than its radius. (In fact the radius $\approx 500\lambda$ where λ is a typical wavelength for the waves detected). We are concerned with the sound field in the horizontal plane passing through the array. The array forms an arc of a circle and is intended to emit a uniform sound field into the sector it faces, as indicated in figure 1.1. We choose axes in this plane centred on the cylinder axis, with the x-axis parallel to the centre of this sector. The height of the array is several times the wavelength. The sound field will have some characteristic vertical variation away

[1]acrylonitrile-butadiene-styrene

from the plane drawn, but this is not of concern to us here. Details of the dimensions and the material properties of the dome are given in Appendix A.

1.3 The Beam Pattern Problem

A standard way of representing the amplitude profile emitted by an array is to plot a beam pattern which is a function of θ, the angle of emission. This beam pattern is proportional to the pressure amplitude heard in the far field at polar angle θ. We will only be considering arrays that respond linearly so we can (by reciprocity) think of this beam pattern as the response of an equivalent receiver array when a plane wave from direction θ is incident on it. We shall describe the beam pattern in terms of this receiver approach.

1.3.1 The Beam Pattern

In order to describe a beam pattern, consider the elements of the array to be at points $\mathbf{x}_j$. Then the pressure at the point $\mathbf{x}_j$ at time t is given by

$$p(\mathbf{x}_j, t) \quad = \quad p_0 e^{-i\omega t} e^{i\mathbf{k}\cdot\mathbf{x}_j} \tag{1.1}$$

where $\mathbf{k}$ is a wave number vector and $\frac{\omega}{2\pi}$ is the frequency of the wave. Of course the physical pressure is the real part of this complex quantity, but since we are looking at a single frequency and the problem is linear, we adopt the usual convention of regarding the physical variables as complex with a time dependence proportional to $e^{-i\omega t}$.

In general, an array responding linearly to the incident field produces an output

$$\begin{aligned} s(t) &= \sum_j w_j p(\mathbf{x}_j, t - \Delta_j) & (1.2) \\ &= \sum_j w_j p_0 e^{-i\omega t} e^{i\omega\Delta_j + i\mathbf{k}\cdot\mathbf{x}_j} & (1.3) \end{aligned}$$

where w_j are shading weights and Δ_j are delays. The time delays are chosen so that waves with $\mathbf{k}$ in the direction of interest sum constructively in this, that is, so that the phases $\omega\Delta_j + \mathbf{k}\cdot\mathbf{x}_j$ are approximately constant as j varies.

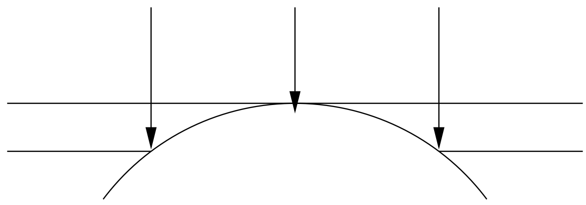

Figure 1.2: A plane wave incident from $\theta = 0$.

For example, if the array were designed to have maximum response to plane waves incident from the $\theta = 0$ direction (as in figure 1.2) we have $\mathbf{k} = (-k, 0)$ and we require

$$\omega\Delta_j - kx_j \quad = \quad \text{const} \quad . \tag{1.4}$$

Hence we need

$$\Delta_j \quad = \quad \frac{x_j}{c} + \text{const} \tag{1.5}$$

where $c = \frac{\omega}{k}$ is the sound speed. Given these Δ_j the array has a peak response of $p_0 \sum_j w_j$.

In our case the aim is for the array to emit wavefronts that are circular arcs, concentric with the array so we have the simpler form $\Delta_j = 0$ for all j.

If we now consider incoming waves from a general angle θ, we have

$$\mathbf{k} \quad = \quad -\frac{\omega}{c}(\cos\theta, \sin\theta) \tag{1.6}$$

and $s(t)$ is of the form

$$s(t) \quad = \quad p_0 e^{-i\omega t} \left(\sum_j w_j \right) D(\theta) \quad . \tag{1.7}$$

$D(\theta)$ is called the directivity of the array, or the beam pattern. Plots of the normalised beam pattern are $20 \log_{10} |D(\theta)| / \max_\theta |D(\theta)|$ against θ in order to measure the beam pattern in decibels (dB). In reality the array consists of 12 or 18 hydrophones each of which averages the pressure over its surface so we aim for an integral average over the arc which we estimate by this sum over j. Hence we need to be sure that the points on the array are spaced finely enough on a wavelength scale to produce an accurate estimate.

Although the design intention of the array is to have $D(\theta)$ approximately constant over the sector $-\alpha_0 \leq \theta \leq \alpha_0$ into which the array faces and much smaller outside that sector, wave interference and the cylinder itself will cause variations from this ideal. As we shall see though, the essential form is maintained, in that $|D(\theta)|$ is large for θ near 0 and small away from that direction. In these circumstances, two important parameters describing the shape of the beam pattern are the beam centre and the beam width.

1.3.2 The Beam Centre

The beam centre, b_c, is defined to be the average value of θ over those directions in which $D(\theta)$ is within 6dB of its maximum. Ideally the beam centre should be at $0°$.

1.3.3 The Beam Width

Let q be the mean power over the sector $3°$ either side of the beam centre. Then the beam width, b_w, is defined to be the width of the sector in which the power is no more than 3dB below q. Ideally the array should have a beam width equal to the angle $2\alpha_0$ of the sector it covers.

1.3.4 Experimental Results

Experiments have been conducted with the sonar set described in section 1.3.1 and they show the beam pattern to have an asymmetric main lobe near $0°$ and a side lobe at about $100°$ which is approximately 15dB down on the main lobe. More detailed experimental results will be given in section 3.1.

1.4 Aims

We would like to be able to produce a mathematical model of the sonar device to enable us to predict the beam pattern produced by such a sonar set and also to find the beam centre and width. Previous models which have been used for the problem did not produce the correct asymmetry and we would like to be able to explain this.

1.5 Outline of Work

In chapter 2 we shall derive two initial models of the situation, one which is a formally complete solution, valid at all frequencies and consisting of an infinite series of Bessel functions, the other being a model motivated by the theory of ray acoustics but only valid at high frequencies. A general introduction to the theory of sound and ray theory can be found in [7] and an introduction to elasticity can be found in [5].

In chapter 3 we study the results from these models and compare them to experimental findings. We shall see that there are some discrepancies between the theoretical and experimental results so in chapter 4 we examine some possible causes for these and in chapter 5 we shall attempt to develop the models to try to reduce the differences with experimental data as well as gaining further insight into the problem.

Chapter 2

Mathematical Models

Here we shall consider two mathematical models for the problem, a mode model and a tangent plane model. In the mode model we let the axis of an infinite cylinder coincide with the z-axis of (x, y, z) space and let a plane sound wave be incident along the negative x-axis. This method produces a formally complete solution for the acoustic pressure field as an infinite series of Bessel functions of integer order and has the advantage of being valid at all frequencies although practically it is most useful for low frequencies since then fewer modes contribute to the sum. The pressure field for a plane wave incident from direction θ is then obtained by rotation about the axis of the cylinder, and hence $D(\theta)$ can be calculated by integrating the pressure over the array.

In the tangent plane model we simplify the problem considerably by looking at an annulus. We replace this annulus by a series of tangents then calculate and superimpose reflection and transmission coefficients. This idea is motivated by the theory of ray acoustics but is only valid at high frequencies. However, as we shall see later, this should not be a problem.

2.1 The Lamé Coefficients

We define the Lamé coefficients of the elastic material to be λ and μ where μ is the shear modulus. A purely elastic isotropic material has (in Cartesian coordinates) a linear stress-strain relation given by

$$\sigma_{ij} = 2\mu e_{ij} + \lambda e_{kk}\delta_{ij} \tag{2.1}$$

where (σ_{ij}) is the stress tensor and (e_{ij}) is the strain tensor. However a visco-elastic material, with stresses σ_{ij} made to vary sinusoidally at radian frequency ω, will have strains also varying at frequency ω (assuming linearity) but not in phase, so if

$$e_{ij} = Re(\hat{e}_{ij} e^{-i\omega t}) \tag{2.2}$$

$$\sigma_{ij} = Re(\hat{\sigma}_{ij} e^{-i\omega t}) \tag{2.3}$$

there is still a relation

$$\hat{\sigma}_{ij} = 2\mu \hat{e}_{ij} + \lambda \hat{e}_{kk} \delta_{ij} \tag{2.4}$$

but λ and μ will now be complex and depend on ω. In [8] it is implied that in plastic materials of this kind, the value of λ can still be taken to be real, the shear modulus having a more significant imaginary part which we will take to be -0.02 times the real part. This figure of -0.02 and the values of λ and μ given in Appendix A are measured values for ABS at the frequency of interest and the fact that the imaginary part of μ is negative corresponds to the fact that the material dissipates energy in shear.

2.2 The Mode Model

The idea behind the mode model comes from the paper written in 1966 by Doolittle and Überall, [2], which summarises the solution to the problem of sound scattering by solid elastic cylinders and also by elastic cylindrical shells both in the case when the fluids inside and outside the shell are identical and when they are different.

Consider an infinite circular cylinder of outer radius a and inner radius b whose axis is the z-axis of the coordinate system. Now let a plane sound wave of circular frequency ω be incident along the negative x-axis as shown in figure 2.1.

We shall denote the fluids outside and inside the cylinder by 1 and 3 respectively, although for our purposes both fluids are the same (water). The elastic material of the cylinder will be denoted by 2 with density ρ_2 and Lamé coefficients λ and μ. The elastic material is assumed to be isotropic and although it is not purely elastic it is still assumed to be linear so the stress-strain hysteresis is just represented by complex

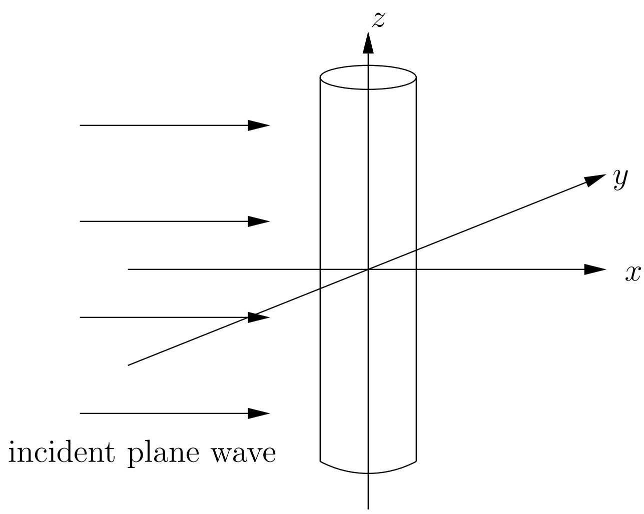

Figure 2.1: The mode model.

values of λ and μ. The speeds of longitudinal and transverse waves in medium 2 are respectively

$$c_L = \left(\frac{\lambda + 2\mu}{\rho_2}\right)^{\frac{1}{2}} \quad (2.5)$$

$$c_T = \left(\frac{\mu}{\rho_2}\right)^{\frac{1}{2}} \quad (2.6)$$

and we write $k_i = \frac{\omega}{c_i}$ for $i = L, T$. In medium i ($i = 1, 3$) the density is ρ_i, the speed of sound is c_i and the propagation constant is $k_i = \frac{\omega}{c_i}$.

2.2.1 Assumptions

In the mode model we make the following assumptions:

- The model assumes we have a 3-D problem in the sense that we model the sonar set in the form of an infinite cylinder. However we assume that the cylinder vibrates in a purely 2-D mode hence the effects of the end caps (which mean that the vertical wavenumber is non zero) are not accounted for.
- Fluid 3 (water) fills the cylinder so the equipment in the cylinder is ignored.
- We assume that sound passes through the array as if it were not there. In reality in figure 2.2 point a hears the sound as the model predicts but the presence of the array distorts the sound so the response at point b is not the same as would

be observed if the array were absent. This is really a special case of the second assumption in that we calculate the response as if not only the other equipment was absent but also as if the array itself were not there.

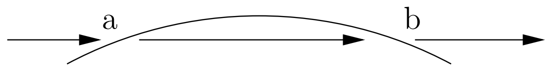

Figure 2.2: Sound passing through array.

- We assume that the array *hears from behind* so in figure 2.3 the sound is heard at point c. This is a similar assumption to the second since one of the main reasons why this is not true in practice is because there is equipment behind the array which prevents the sound reaching it without being distorted.

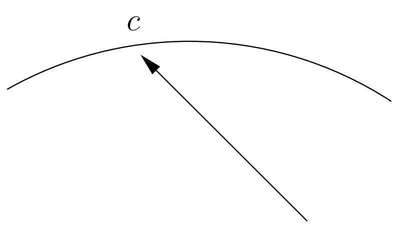

Figure 2.3: The array hears from behind.

- The model allows for all reflections off the sides of the cylinder.

2.2.2 The Series Solution

Henceforth we shall adopt a cylindrical coordinate system

$$x = r\cos\theta \tag{2.7}$$

$$y = r\sin\theta \tag{2.8}$$

$$z = z\ . \tag{2.9}$$

We express the pressure in medium 1 as a solution of the wave equation

$$c_1^2\nabla^2 p = \frac{\partial^2 p}{\partial t^2} \tag{2.10}$$

in the form $p = p_i + p_s$ where p_i is an incident plane wave pressure and p_s is a scattered pressure (that is to say, an outgoing wave). By separating variables we find that the time dependence is of the form $e^{-i\omega t}$ and to find the spatial dependence we must solve the Helmholtz equation

$$\nabla^2 p + k^2 p = 0 \ . \tag{2.11}$$

Since the pressure must be symmetric about $\theta = 0$, we find

$$p_i = p_0 e^{-i\omega t} \sum_{n=0}^{\infty} i^n \epsilon_n J_n(k_1 r) \cos n\theta \tag{2.12}$$

$$p_s = p_0 e^{-i\omega t} \sum_{n=0}^{\infty} i^n \epsilon_n b_n H_n^{(1)}(k_1 r) \cos n\theta \tag{2.13}$$

where $\epsilon_n = (2 - \delta_{n0})$, J_n are Bessel functions of the first kind, $H_n^{(1)}$ are Hankel functions and b_n are constants to be determined. Note that $H_n^{(1)}$ terms appear in (2.13) rather than $H_n^{(2)}$ in order that p_s represents outgoing waves in the far field. The radial displacements at $r = a$ are thus given by

$$(u_i + u_s)_r = \frac{1}{\rho_1 \omega^2} \frac{\partial}{\partial r}(p_i + p_s) \ . \tag{2.14}$$

In medium 2 the displacement vector $\mathbf{u}$ must satisfy the equations which govern linear elasticity, that is the Navier equations

$$\rho_2 \frac{\partial^2 \mathbf{u}}{\partial t^2} = (\lambda + 2\mu)\nabla(\nabla \cdot \mathbf{u}) - \mu \nabla \wedge (\nabla \wedge \mathbf{u}) \ . \tag{2.15}$$

Writing $\mathbf{u} = -\nabla\Psi + \nabla \wedge \mathbf{A}$ and substituting into (2.15) we see that the scalar potential Ψ describing compressive waves must satisfy

$$\frac{1}{c_L^2} \frac{\partial^2 \Psi}{\partial t^2} = \nabla^2 \Psi \tag{2.16}$$

and the vector potential $\mathbf{A}$ describing shear waves must satisfy

$$\frac{1}{c_T^2} \frac{\partial^2 \mathbf{A}}{\partial t^2} = \nabla^2 \mathbf{A} \ . \tag{2.17}$$

The problem is infinite in the z-direction so $A_r = A_\theta = 0$ (and hence $u_z = 0$) and we have

$$\Psi = p_0 e^{-i\omega t} \sum_{n=0}^{\infty} i^n \epsilon_n \left(c_n J_n\left(k_L r\right) + d_n Y_n\left(k_L r\right)\right) \cos n\theta \tag{2.18}$$

$$A_z = p_0 e^{-i\omega t} \sum_{n=0}^{\infty} i^n \epsilon_n \left(e_n J_n\left(k_T r\right) + f_n Y_n\left(k_T r\right)\right) \sin n\theta \ . \tag{2.19}$$

Only cosine terms appear in (2.18) since pressure and displacement must be symmetric about $\theta = 0$. However in order that the displacement may be symmetric about $\theta = 0$ the vector potential must be anti-symmetric and hence only sine terms appear in (2.19).

In medium 3 we have a compressive wave and since this must be regular at the origin only Bessel functions of the first kind are included so

$$p_3 = p_0 e^{-i\omega t} \sum_{n=0}^{\infty} i^n \epsilon_n g_n J_n(k_3 r) \cos n\theta \ . \tag{2.20}$$

We are now required to find the unknown coefficients, b_n, c_n, d_n, e_n, f_n and g_n. These can be determined using the boundary conditions which hold at both interfaces, $r = a$ and $r = b$.

- The pressure in the fluid must be equal to minus the normal component of stress in the solid.
- The normal component of displacement must be continuous.
- The tangential components of shearing stress must be zero.

As in [3] we can express the stress components in cylindrical coordinates as

$$\sigma_{rr} = -\lambda \nabla^2 \Psi + 2\mu \frac{\partial u_r}{\partial r} \tag{2.21}$$

$$\sigma_{r\theta} = \mu \left(\frac{1}{r} \frac{\partial u_r}{\partial \theta} + r \frac{\partial}{\partial r} \left(\frac{u_\theta}{r} \right) \right) \tag{2.22}$$

$$\sigma_{rz} = \mu \left(\frac{\partial u_r}{\partial z} + \frac{\partial u_z}{\partial r} \right) \ . \tag{2.23}$$

Because of the conditions of symmetry imposed, $\sigma_{rz} = 0$ automatically holds. This means that the boundary conditions are

$$\lambda \nabla^2 \Psi - 2\mu \frac{\partial u_r}{\partial r} = p_i + p_s \qquad \text{at } r = a \tag{2.24}$$

$$\lambda \nabla^2 \Psi - 2\mu \frac{\partial u_r}{\partial r} = p_3 \qquad \text{at } r = b \tag{2.25}$$

$$(u_i + u_s)_r = u_r \qquad \text{at } r = a, b \tag{2.26}$$

$$\frac{\partial u_r}{\partial \theta} + r \frac{\partial u_\theta}{\partial r} - u_\theta = 0 \qquad \text{at } r = a, b \ . \tag{2.27}$$

Applying these boundary conditions and writing $x_i = ak_i$, $y_i = bk_i$ gives a linear system to be solved to find the coefficients,

$$\begin{pmatrix} \alpha_{11} & \alpha_{12} & \alpha_{13} & \alpha_{14} & \alpha_{15} & 0 \\ \alpha_{21} & \alpha_{22} & \alpha_{23} & \alpha_{24} & \alpha_{25} & 0 \\ 0 & \alpha_{32} & \alpha_{33} & \alpha_{34} & \alpha_{35} & 0 \\ 0 & \alpha_{42} & \alpha_{43} & \alpha_{44} & \alpha_{45} & \alpha_{46} \\ 0 & \alpha_{52} & \alpha_{53} & \alpha_{54} & \alpha_{55} & \alpha_{56} \\ 0 & \alpha_{62} & \alpha_{63} & \alpha_{64} & \alpha_{65} & 0 \end{pmatrix} \begin{pmatrix} b_n \\ c_n \\ d_n \\ e_n \\ f_n \\ g_n \end{pmatrix} = \begin{pmatrix} \beta_1 \\ \beta_2 \\ 0 \\ 0 \\ 0 \\ 0 \end{pmatrix}. \tag{2.28}$$

The coefficients α_{ij} and β_j are defined as follows

$$\alpha_{11} = -\left(\frac{x_1}{k_1}\right)^2 H_n^{(1)}(x_1) \tag{2.29}$$

$$\alpha_{12} = 2\mu x_L^2 J_n''(x_L) - \lambda x_L^2 J_n(x_L) \tag{2.30}$$

$$\alpha_{13} = 2\mu x_L^2 Y_n''(x_L) - \lambda x_L^2 Y_n(x_L) \tag{2.31}$$

$$\alpha_{14} = 2\mu n(J_n(x_T) - x_T J_n'(x_T)) \tag{2.32}$$

$$\alpha_{15} = 2\mu n(Y_n(x_T) - x_T Y_n'(x_T)) \tag{2.33}$$

$$\beta_1 = \left(\frac{x_1}{k_1}\right)^2 J_n(x_1) \tag{2.34}$$

$$\alpha_{21} = -x_1 H_n^{(1)'}(x_1) \tag{2.35}$$

$$\alpha_{22} = -\rho_1\omega^2 x_L J_n'(x_L) \tag{2.36}$$

$$\alpha_{23} = -\rho_1\omega^2 x_L Y_n'(x_L) \tag{2.37}$$

$$\alpha_{24} = \rho_1\omega^2 n J_n(x_T) \tag{2.38}$$

$$\alpha_{25} = \rho_1\omega^2 n Y_n(x_T) \tag{2.39}$$

$$\beta_2 = x_1 J_n'(x_1) \tag{2.40}$$

$$\alpha_{32} = 2n(x_L J_n'(x_L) - J_n(x_L)) \tag{2.41}$$

$$\alpha_{33} = 2n(x_L Y_n'(x_L) - Y_n(x_L)) \tag{2.42}$$

$$\alpha_{34} = -x_T^2 J_n''(x_T) + x_T J_n'(x_T) - n^2 J_n(x_T) \tag{2.43}$$

$$\alpha_{35} = -x_T^2 Y_n''(x_T) + x_T Y_n'(x_T) - n^2 Y_n(x_T) \tag{2.44}$$

$$\alpha_{42} = 2\mu y_L^2 J_n''(y_L) - \lambda y_L^2 J_n(y_L) \tag{2.45}$$

$$\alpha_{43} = 2\mu y_L^2 Y_n''(y_L) - \lambda y_L^2 Y_n(y_L) \tag{2.46}$$

$$\alpha_{44} = 2\mu n(J_n(y_T) - y_T J_n'(y_T)) \tag{2.47}$$

$$\alpha_{45} = 2\mu n(Y_n(y_T) - y_T Y_n'(y_T)) \tag{2.48}$$

$$
\begin{aligned}
\alpha_{46} &= -\left(\frac{y_3}{k_3}\right)^2 J_n(y_3) && (2.49)\\
\alpha_{52} &= -\rho_3\omega^2 y_L J_n'(y_L) && (2.50)\\
\alpha_{53} &= -\rho_3\omega^2 y_L Y_n'(y_L) && (2.51)\\
\alpha_{54} &= \rho_3\omega^2 n J_n(y_T) && (2.52)\\
\alpha_{55} &= \rho_1\omega^2 n Y_n(y_T) && (2.53)\\
\alpha_{56} &= -y_3 J_n'(y_3) && (2.54)\\
\alpha_{62} &= 2n(y_L J_n'(y_L) - J_n(y_L)) && (2.55)\\
\alpha_{63} &= 2n(y_L Y_n'(y_L) - Y_n(y_L)) && (2.56)\\
\alpha_{64} &= -y_T^2 J_n''(y_T) + y_T J_n'(y_T) - n^2 J_n(y_T) && (2.57)\\
\alpha_{65} &= -y_T^2 Y_n''(y_T) + y_T Y_n'(y_T) - n^2 Y_n(y_T) \quad . && (2.58)
\end{aligned}
$$

2.2.3 Calculating the Beam Pattern by the Mode Method

Having calculated the coefficients g_n we can calculate the pressure at any point (r, θ) inside the cylinder due to a wave incident along the negative x-axis as

$$
p_3(r,\theta) = p_0 e^{-i\omega t} \sum_{n=0}^{\infty} i^n \epsilon_n g_n J_n(k_3 r) \cos n\theta \quad . \tag{2.59}
$$

Hence the pressure at (r, θ') due to a wave from θ is given by $p_3(r, \theta' - \theta)$. We can then calculate the beam pattern by defining the points on the array as $(r_j \cos\theta_j, r_j \sin\theta_j)$, $j = 0, \ldots, m$. Then the beam pattern is given by

$$
\begin{aligned}
D(\theta) &= \sum_{j=0}^{m} w_j p_3(r_j, \theta_j - \theta) && (2.60)\\
&= \sum_{j=0}^{m} w_j \sum_{n=0}^{\infty} i^n \epsilon_n g_n J_n(k_3 r_j) \cos n(\theta_j - \theta) \quad . && (2.61)
\end{aligned}
$$

We shall choose $w_j = 1$ throughout so that the array is unshaded.

2.3 The Tangent Plane Approximation

We now consider an annulus as a 2-D model of the cylinder and then replace it by a series of tangents at which we calculate reflection and transmission coefficients. This is a ray theory model and a sound ray incident on the cylinder is assumed to be reflected and transmitted as if it had been incident on a flat plate of ABS, of thickness $h = a - b$, tangent to the cylinder at the point of incidence.

2.3.1 Assumptions

In the simplest tangent plane approximation we assume:

- The model of the cylinder as an annulus is equivalent to that of an infinite cylinder in that we assume vibrations are in a purely 2-D mode, so in the same way as in the mode model the effects of the end caps cannot be accounted for.
- We assume the cylinder is filled with water so the equipment in the cylinder is ignored.
- We assume that sound passes through the array as if it were not there. (As in the mode model).
- We assume that the array hears from behind. (As in the mode model).
- The model does not take account of the fact that waves reflect off the walls of the cylinder if they do not hit the array first.

2.3.2 Calculation of the Reflection and Transmission Coefficients

We let the solid layer of thickness h $(= a - b)$ occupy the strip $0 \leq y \leq h$ and we let a sound wave hit the solid at $y = h$ with an angle of incidence ϕ. There is then a reflected wave in $y > h$ and a transmitted wave in $y < 0$ with reflection and transmission coefficients R and T respectively as in figure 2.4. (Note that the axes in figure 2.4 are temporary, they are not the main axes used for the whole sonar set).

Hence the pressure in the water for $y > h$ is

$$p = p_0 e^{-i\omega t} e^{ikx} e^{-ily} + R p_0 e^{-i\omega t} e^{ikx} e^{ily} \tag{2.62}$$

and for $y < 0$

$$p = T p_0 e^{-i\omega t} e^{ikx} e^{-ily} \tag{2.63}$$

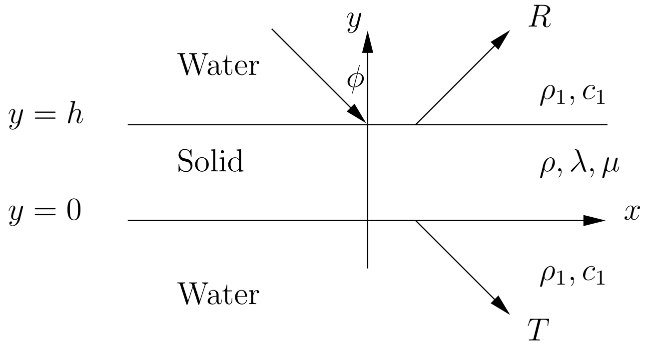

Figure 2.4: A wave hitting the solid layer giving a reflected and a transmitted wave.

where $k = k_1 \sin\phi$, $l = k_1 \cos\phi$ and $k_1 = \omega/c_1$. In the solid layer the displacement $\mathbf{u}$ is given by

$$\begin{pmatrix} u \\ v \end{pmatrix} = e^{-i\omega t} e^{ikx} \sum_{j=1}^{4} a_j \begin{pmatrix} u_j \\ v_j \end{pmatrix} e^{il_j y} \tag{2.64}$$

where for shear waves

$$l_j^2 = \frac{\rho\omega^2}{\mu} - k^2 \tag{2.65}$$

$$\begin{pmatrix} u_j \\ v_j \end{pmatrix} = \begin{pmatrix} l_j \\ -k \end{pmatrix} \qquad j = 1, 2 \tag{2.66}$$

and for compressive waves

$$l_j^2 = \frac{\rho\omega^2}{\lambda + 2\mu} - k^2 \tag{2.67}$$

$$\begin{pmatrix} u_j \\ v_j \end{pmatrix} = \begin{pmatrix} k \\ l_j \end{pmatrix} \qquad j = 3, 4 \ . \tag{2.68}$$

The a_j are constants to be determined, the other two unknowns are R and T which can be found using the boundary conditions which hold at each interface ($y = 0$ and $y = h$)

- The displacements in the y-direction must be continuous.
- The normal component of stress in the solid must equal minus the pressure in the fluid.
- The tangential components of stress must be zero.

The stress tensor is defined by

$$\sigma_{ij} = \lambda \frac{\partial u_k}{\partial x_k}\delta_{ij} + \mu\left(\frac{\partial u_i}{\partial x_j} + \frac{\partial u_j}{\partial x_i}\right) \quad . \tag{2.69}$$

So

$$\sigma_{yy} = (\lambda + 2\mu)\frac{\partial v}{\partial y} + \lambda\frac{\partial u}{\partial x} \tag{2.70}$$

$$\sigma_{xy} = \mu\left(\frac{\partial u}{\partial y} + \frac{\partial v}{\partial x}\right) \tag{2.71}$$

are respectively the normal and tangential components of stress in the solid.

Writing

$$(\sigma_{yy})_j = (\lambda + 2\mu) i l_j v_j + \lambda i k u_j \tag{2.72}$$

$$(\sigma_{xy})_j = \mu\left(i l_j u_j + i k v_j\right) \tag{2.73}$$

$$\alpha_j = \left(\frac{\rho_1\omega^2}{p_0}\right) a_j \tag{2.74}$$

we get a linear system to solve to find the unknowns R, T, α_j,

$$\begin{bmatrix} il & 0 & -v_1 e^{il_1 h} & -v_2 e^{il_2 h} & -v_3 e^{il_3 h} & -v_4 e^{il_4 h} \\ 0 & il & v_1 & v_2 & v_3 & v_4 \\ 1 & 0 & \frac{(\sigma_{yy})_1 e^{il_1 h}}{\rho_1\omega^2} & \frac{(\sigma_{yy})_2 e^{il_2 h}}{\rho_1\omega^2} & \frac{(\sigma_{yy})_3 e^{il_3 h}}{\rho_1\omega^2} & \frac{(\sigma_{yy})_4 e^{il_4 h}}{\rho_1\omega^2} \\ 0 & 1 & \frac{(\sigma_{yy})_1}{\rho_1\omega^2} & \frac{(\sigma_{yy})_2}{\rho_1\omega^2} & \frac{(\sigma_{yy})_3}{\rho_1\omega^2} & \frac{(\sigma_{yy})_4}{\rho_1\omega^2} \\ 0 & 0 & \frac{(\sigma_{xy})_1 e^{il_1 h}}{\rho_1\omega^2} & \frac{(\sigma_{xy})_2 e^{il_2 h}}{\rho_1\omega^2} & \frac{(\sigma_{xy})_3 e^{il_3 h}}{\rho_1\omega^2} & \frac{(\sigma_{xy})_4 e^{il_4 h}}{\rho_1\omega^2} \\ 0 & 0 & \frac{(\sigma_{xy})_1}{\rho_1\omega^2} & \frac{(\sigma_{xy})_2}{\rho_1\omega^2} & \frac{(\sigma_{xy})_3}{\rho_1\omega^2} & \frac{(\sigma_{xy})_4}{\rho_1\omega^2} \end{bmatrix} \begin{bmatrix} Re^{ilh} \\ T \\ \alpha_1 \\ \alpha_2 \\ \alpha_3 \\ \alpha_4 \end{bmatrix} = \begin{bmatrix} ile^{-ilh} \\ 0 \\ -e^{-ilh} \\ 0 \\ 0 \\ 0 \end{bmatrix} \tag{2.75}$$

Notes

When λ and μ are purely real the problem is symmetric so $|T \pm Re^{ilh}| = 1$ and $|T|^2 + |R|^2 = 1$. (This corresponds to the case when the scatterer is purely elastic and it dissipates no energy).

When μ is complex $|T \pm Re^{ilh}| < 1$ and $|T|^2 + |R|^2 < 1$ for $-\frac{\pi}{2} < \phi < \frac{\pi}{2}$. (Complex μ correspond to the dissipation of energy in the layer).

2.3.3 Calculating the Beam Pattern by the Tangent Plane Method

For incoming sound from θ, arriving at the point $\mathbf{x}_j$ on the array, the angle of incidence on the cylinder is ϕ as in figure 2.5.

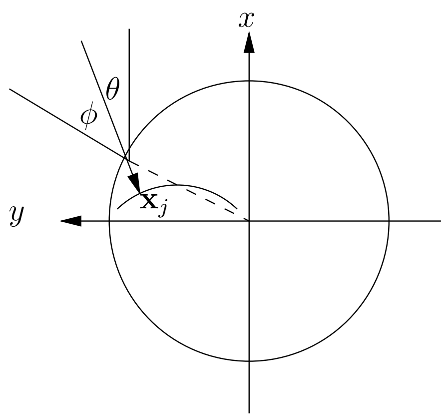

Figure 2.5: A wave incident on the annulus.

In order to define the elements, $\mathbf{x}_j$, of the array, let $\mathbf{x}_c$ be the mid-point of the array, L its length and R its radius. Then

$$
\begin{aligned}
x_j &= x_c - R + R\cos\alpha_j && (2.76)\\
y_j &= y_c + R\sin\alpha_j && (2.77)\\
\text{where}\quad \alpha_0 &= \frac{L}{2R} && (2.78)\\
\alpha_n &= -\alpha_0 && (2.79)\\
\alpha_j &= \alpha_0 + j\frac{\alpha_n - \alpha_0}{n} \qquad j = 0, 1, \ldots, n\ . && (2.80)
\end{aligned}
$$

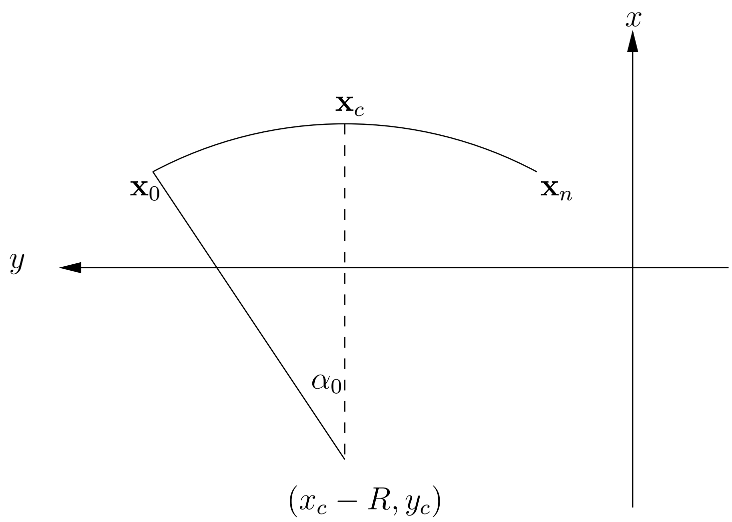

Figure 2.6: The angle α_0.

The incident wave has

$$
p_i = p_0 e^{-i\omega t} e^{-ik_1(x\cos\theta + y\sin\theta)} \qquad \text{where } k_1 = \frac{\omega}{c_1}\ . \tag{2.81}
$$

If $T(\phi)$ is known, the tangent plane method approximates the response at $\mathbf{x}_j$ by

$$s_j(t) = T(\phi) p_0 e^{-i\omega t} e^{-ik_1(x_j\cos\theta + y_j\sin\theta)} \quad . \tag{2.82}$$

Hence the response of the array is

$$\begin{aligned} s(t) &= \sum_j w_j s_j(t - \Delta_j) && (2.83)\\ &= p_0 e^{-i\omega t} D(\theta) \quad . && (2.84) \end{aligned}$$

Since the idea is for the array to emit a spherically spreading wave, we choose $\Delta_j = 0$ and then the beam pattern is given by

$$D(\theta) = \sum_j w_j e^{-ik_1(x_j\cos\theta + y_j\sin\theta)} T(\phi) \quad . \tag{2.85}$$

So in order to evaluate this we simply need to find ϕ for any given angle θ and point $\mathbf{x}_j$ on the array.

Given θ and $\mathbf{x}_j$ we let $\tilde{\mathbf{x}}$ be the point where the wave from θ through $\mathbf{x}_j$ enters the cylinder. Then

$$\begin{aligned} \tilde{x} &= x_j + \beta\cos\theta && (2.86)\\ \tilde{y} &= y_j + \beta\sin\theta && (2.87) \end{aligned}$$

where β is the distance from $\tilde{\mathbf{x}}$ to $\mathbf{x}_j$ and is given by

$$\beta = -(x_j\cos\theta + y_j\sin\theta) + \sqrt{b^2 - (y_j\cos\theta - x_j\sin\theta)^2} \quad . \tag{2.88}$$

From this we deduce that

$$\phi = \sin^{-1}\left(\frac{y_j\cos\theta - x_j\sin\theta}{b}\right) \tag{2.89}$$

and hence $D(\theta)$ can be evaluated for any θ.

Note that although the inner radius b is used in the calculation of ϕ, since h/a is small it will not crucially affect things whether we use a or b.

Chapter 3

Results of the Models

3.1 Experimental Results

The following experimental results are reproduced with the kind permission of Thomson Marconi Sonar Systems Ltd.

In figure 3.1 the beam pattern is plotted for the whole range of θ and we see there is a main lobe centred near $0°$ and a side lobe at about $100°$ which is about 15dB down on the main lobe. The width of the main beam is approximately $10°$ and the beam centre is at $-2°$. The spiked graph is the actual beam pattern produced, while the other is a smoothed plot.

3.2 Results from the Mode Model

The beam pattern produced by the mode model is given by

$$D(\theta) \quad = \quad \sum_{j=0}^{m} w_j \sum_{n=0}^{\infty} i^n \epsilon_n g_n J_n(k_3 r_j) \cos n(\theta_j - \theta) \quad . \tag{3.1}$$

We shall truncate the series by summing from $n = 0$ to N, the values of N being considered here are $N = 600$ and 1000. Computations summing further terms show no significant alterations to the beam pattern obtained by summing the first 1001 terms.

The subsequent beam patterns produced are plotted in figure 3.2. The top left plot has μ real and $N = 600$, top right has $N = 1000$, the bottom left and right plots have μ complex and $N = 600$ and $N = 1000$ respectively.

We take uniform shading (that is $w_j = 1$, $j = 0, \ldots, m$) and we shall consider the case when there are 414 equally spaced points on the array (414 being the nearest

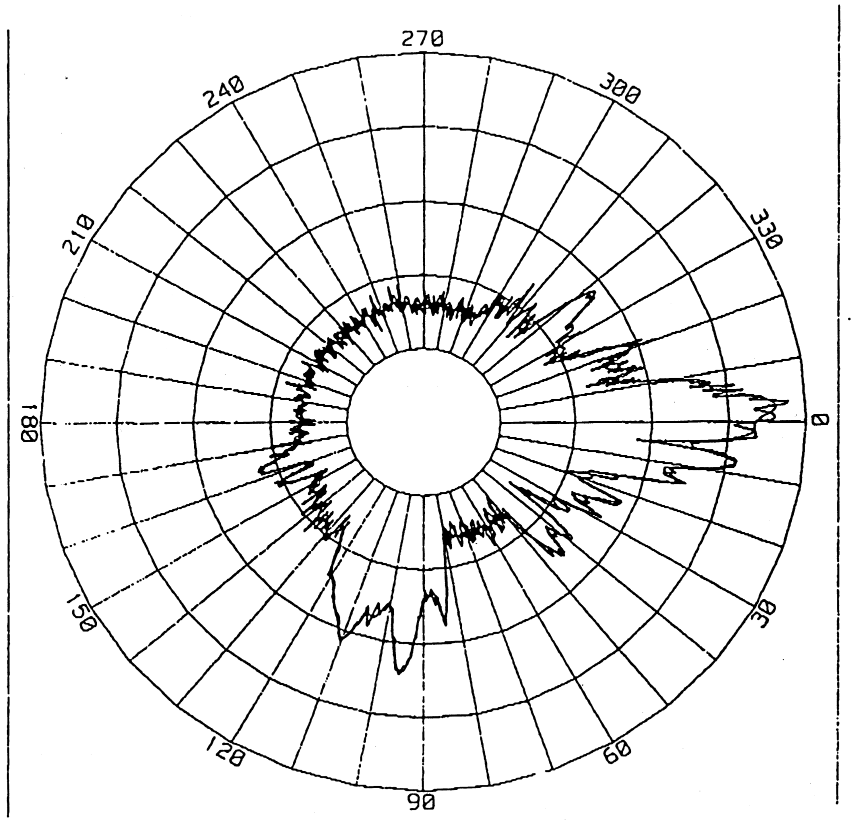

Figure 3.1: The beam pattern produced by experimental data.

integer above $\frac{6Lf}{c_1}$). We calculate the beam pattern for a discrete set of 1000 points, θ, between $\pm 100°$.

From the plots in figure 3.2 we see that with 600 terms in the sum the beam pattern has a main lobe near 0° and a side lobe centred at about −50°, about 13dB down on the main lobe. The main lobe is not symmetric and it has a dip in the middle of about 3dB in the real case and about 2dB in the complex case. There is a noticeable difference between the graphs for 600 and 1000 terms, for the larger sum the main lobe has four peaks, the largest being centred on 0°. In addition to the side lobe at −50° there is a slightly larger lobe at about −70° and one at −100° which is about 15dB down on the main lobe. Also there is a spike at 30°, about 16dB down on the main lobe in the real case and about 19dB down in the complex.

The beam centres and beam widths are given in table 3.1 and from this we see that when $N = 1000$ the beam width is almost 1.5 times that for the case $N = 600$ and the beam centres are further offset from 0° for the smaller sum.

μ	N	beam centre	beam width
real	600	$-2.4°$	$7.724°$
real	1000	$-1.2°$	$10.57°$
complex	600	$-2.6°$	$7.772°$
complex	1000	$-1°$	$10.75°$

Table 3.1: Values of the beam centre and beam width given by the mode model.

Clearly the truncation of the series at 600 terms leads to a beam pattern which is in closer agreement with the experimentally observed asymmetry than the full 1000 term series. Explaining this fact is another aim of the work in addition to those aims already mentioned in section 1.4.

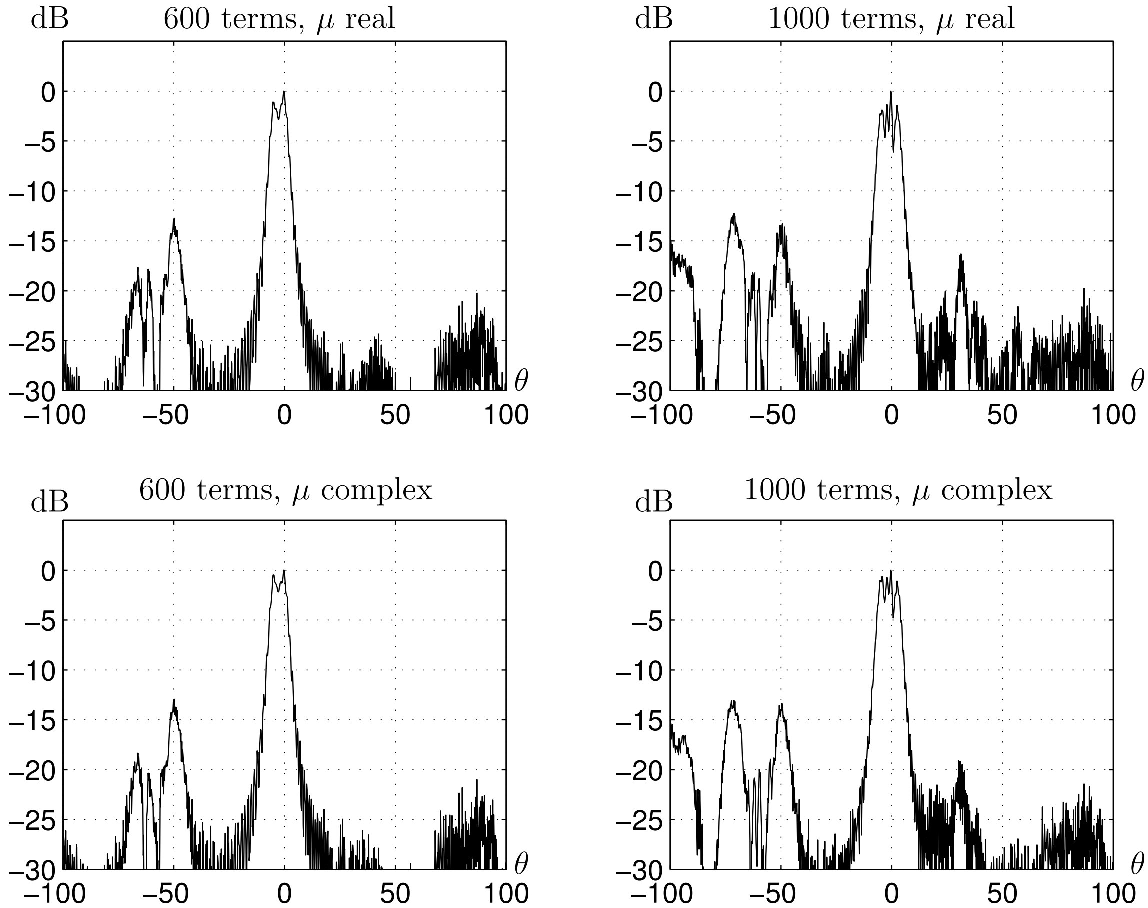

Figure 3.2: The beam patterns produced by the mode method.

3.3 Results from the Tangent Plane Model

3.3.1 The Transmission Coefficients

First of all we consider the modulus of the transmission coefficient (calculated in section 2.3.2) in the cases when μ is real and complex. When μ is real we see that since for shear waves

$$l_j \;=\; \pm\sqrt{\frac{\rho\omega^2}{\mu} - k^2} \tag{3.2}$$

the l_j for shear waves are always real. However for compressive waves

$$l_j \;=\; \pm\sqrt{\frac{\rho\omega^2}{\lambda + 2\mu} - k^2} \tag{3.3}$$

which is only real for $|\sin\phi| < \frac{1500}{2172}$ (which is the ratio of the velocity of sound in water to the compressive wave velocity) that is, within 43.675° of normal incidence. Hence in a plot of $|T|$ (figure 3.3 top left) we see compressive motion decaying through the layer beyond 43.675°. The dissipation modelled by including some imaginary component of μ modifies the detail of $|T(\phi)|$ but it retains the feature that there is a critical angle of incidence near 43° where the transmission is drastically reduced. (See figure 3.3 top right).

3.3.2 The Beam Pattern

The beam pattern is again plotted for a discrete set of values of θ, ranging from $-100°$ to 100°, 400 points being taken in all. Again 414 equally spaced points on the array were used as defined by (2.76) - (2.80).

On plotting the beam pattern (in figure 3.3 bottom left for real μ and bottom right for complex μ) we again see that there is a main lobe centred about $-1.7°$ with a beam width of 8.7°. There are depressions at $\theta = \pm 90°$ and it is found that these become deeper if less points on the array are sampled. As in the mode model the main lobe is not symmetric though this time the main lobe appears to have 3 distinct peaks.

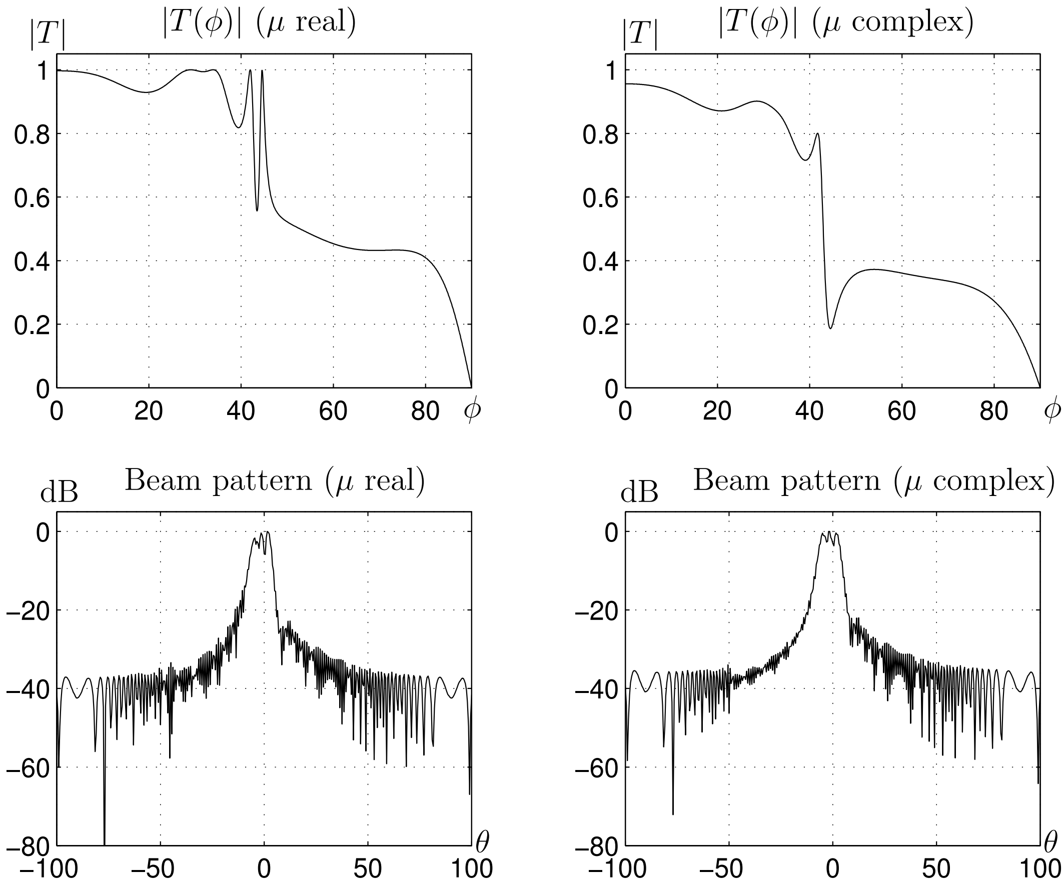

Figure 3.3: Absolute values of transmission coefficients and beam patterns produced by the tangent plane method.

3.3.3 The Beam Width

Experimentally the set has been tested with various positions for the array centre, in particular moving it in the y-direction. Hence in figure 3.4 the beam width is plotted against the value of y_c for fixed values of x_c, R and L the beam width having been calculated by the tangent plane method. We see that the beam width changes with y_c, the beam being widest for the smallest value of y_c and the width varying between $8.5°$ and $13°$. On performing a similar calculation for values of x_c between 0.1 and 0.2 it can be seen that the beam width only varies between $8.7°$ and $9.4°$ so the changes are not as dramatic.

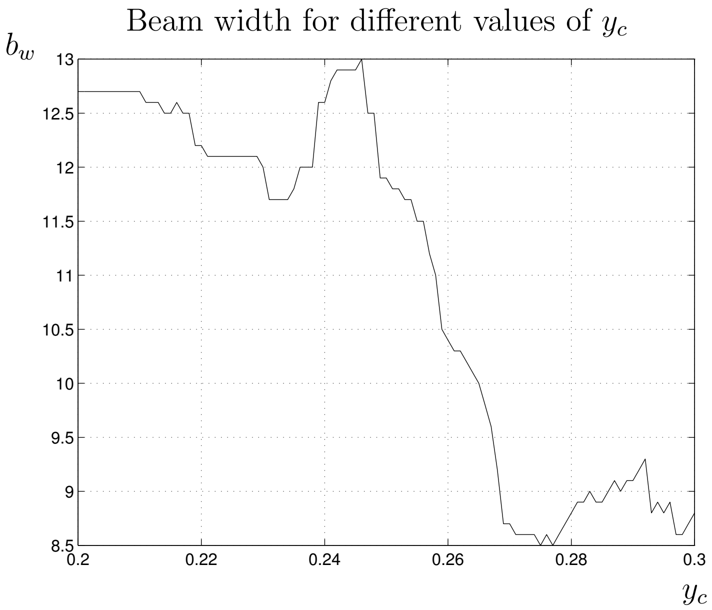

Figure 3.4: The beam width for $0.2 \leq y_c \leq 0.3$.

3.4 Explanation of the Asymmetry of the Tangent Plane Model

The results of the tangent plane approximation show that this method produces the right kind of asymmetry in the main lobe of the beam pattern and the reasons for this can be explained using the method of stationary phase.

We define a general point (x, y) on the array by

$$x = x_c - R + R\cos\alpha \tag{3.4}$$

$$y = y_c + R\sin\alpha \tag{3.5}$$

and we define α_0 as in (2.78). Then in the absence of the cylinder, the array gain function is

$$g = \frac{1}{2\alpha_0}\int_{-\alpha_0}^{\alpha_0} e^{-ik_1(x\cos\theta + y\sin\theta)}d\alpha \tag{3.6}$$

$$= \frac{1}{2\alpha_0}e^{-ik_1(x_c-R)\cos\theta}e^{-ik_1y_c\sin\theta}\int_{-\alpha_0}^{\alpha_0} e^{-ik_1R\cos(\alpha-\theta)}d\alpha\ . \tag{3.7}$$

k_1R is a large parameter (in excess of 1450) so we can estimate the integral, I, using the method of stationary phase. Restricting θ to the range $[-\frac{\pi}{2}, \frac{\pi}{2}]$ there is only a point of stationary phase (given by $\alpha = \theta$) when $\theta \in [-\alpha_0, \alpha_0]$. When θ is outside this range, $I \sim O(k_1R)^{-1}$. If $\theta \in [-\alpha_0, \alpha_0]$ the main contribution to the integral comes from near $\alpha = \theta$ so we can write

$$I \sim \int_{\theta-\epsilon}^{\theta+\epsilon} e^{-ik_1R\cos(\alpha-\theta)} d\alpha \quad . \tag{3.8}$$

Expanding $\cos(\alpha - \theta)$ in a Taylor series and putting $\alpha - \theta = \epsilon p$ gives

$$I \sim e^{-ik_1R} \int_{-1}^{1} e^{\frac{1}{2}ik_1R\epsilon^2p^2} \epsilon dp \quad . \tag{3.9}$$

We can now extend the range of integration since this only re-introduces a small error to give

$$I \sim e^{-ik_1R} \int_{-\infty}^{\infty} e^{\frac{1}{2}ik_1R\epsilon^2p^2} \epsilon dp \quad . \tag{3.10}$$

Integrating round the contour γ shown in figure 3.5 yields

$$I \sim (1+i)e^{-ik_1R}\sqrt{\frac{\pi}{k_1R}} \quad = \quad e^{-ik_1R}\sqrt{\frac{2\pi i}{k_1R}} \tag{3.11}$$

which determines the approximately constant gain of the array in the range $|\theta| < \alpha_0$.

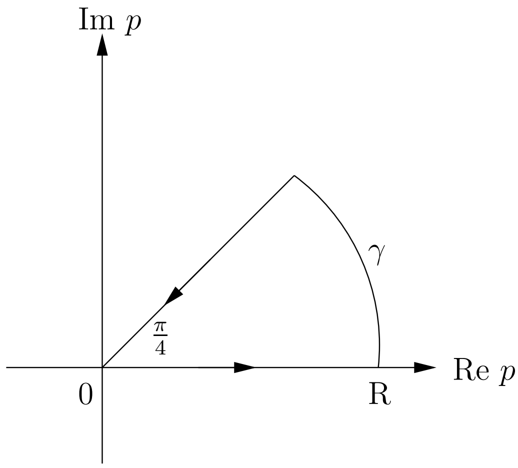

Figure 3.5: The contour γ.

The change in behaviour of the gain of the array from $O(k_1R)^{-\frac{1}{2}}$ to $O(k_1R)^{-1}$ near $\pm\alpha_0$ is governed by the speed of convergence of the integral to which the main contribution comes from the values of α near θ, say the region in which the phase differs by $\approx \frac{\pi}{2}$ from its stationary value. This is given by

$$k_1R(1 - \cos(\alpha - \theta)) \approx \frac{\pi}{2} \tag{3.12}$$

$$\Rightarrow |\alpha - \theta| \approx \sqrt{\frac{\pi}{k_1R}} \approx 2.5^\circ \quad . \tag{3.13}$$

So in the absence of the shell, the gain is symmetric about $\theta = 0$ and of the form shown in figure 3.6.

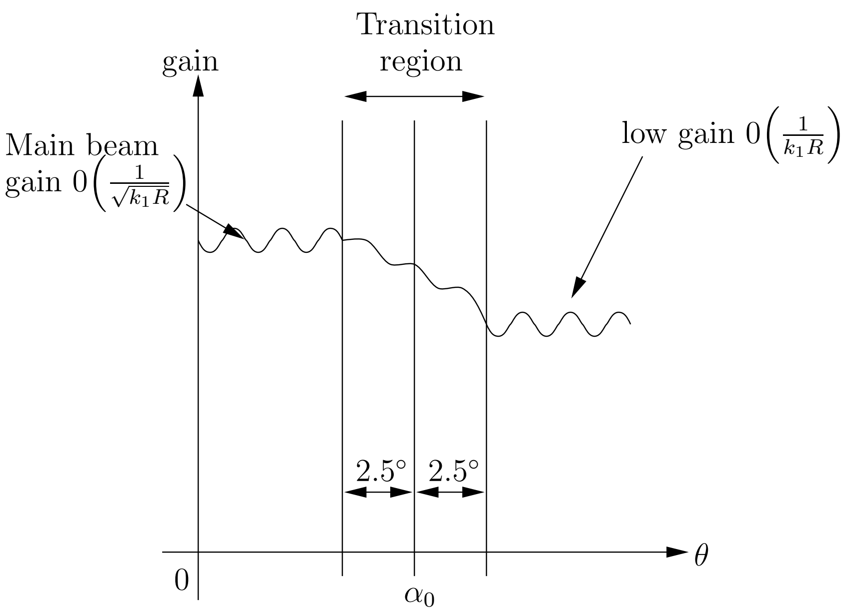

Figure 3.6: The form of the gain of the array in the absence of the shell.

With the shell the gain is given by

$$g = \frac{1}{2\alpha_0}\int_{-\alpha_0}^{\alpha_0} T(\phi)e^{-ik_1R(x\cos\theta+y\sin\theta)}d\alpha \quad . \tag{3.14}$$

In spite of the extra factor, the same basic idea should hold, that the main contribution comes from α near to θ and specifically within $O(k_1R)^{-\frac{1}{2}}$ of θ.

If we compare the main contributions for $\theta = \pm 5°$ we see that when $\theta = +5°$ the passage through the shell is much more oblique. In fact the relevant ϕ values are

$\theta = 5°$		$\theta = -5°$	
$\alpha = 2.5°$	$\phi = 34.2°$	$\alpha = -7.5°$	$\phi = 18.6°$
$\alpha = 5°$	$\phi = 39.6°$	$\alpha = -5°$	$\phi = 23.1°$
$\alpha = 7.5°$	$\phi = 45.0°$	$\alpha = -2.5°$	$\phi = 27.8°$

So for $\theta = +5°$ part of the region of the array that is supposed to be giving the main contribution to the integral is being severely affected by the cut off in T for $\phi > 43.675°$.

We have also seen that the form of the main beam is particularly sensitive to changes in the value of y_c. This is because a large value of y_c makes the relevant rays more obliquely incident and hence more severely affected by the shell transmission.

Experimental evidence backs up this theory, in figure 3.7 the measured beam pattern is plotted with and without the dome. Without the dome the beam pattern appears almost symmetric, but the beam pattern with the dome in position is markedly asymmetric.

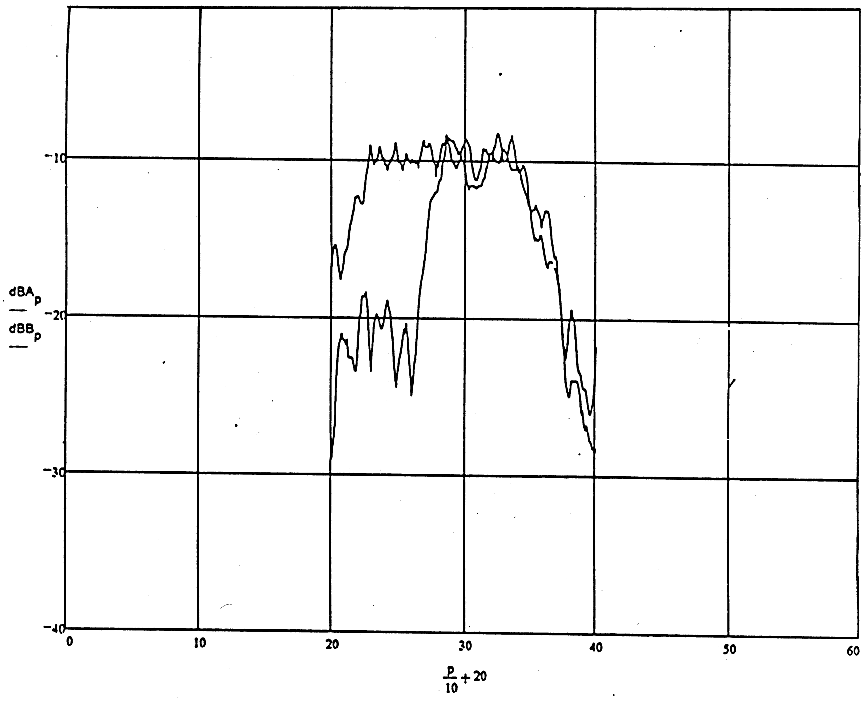

Figure 3.7: The measured beam pattern with and without the dome.

3.5 Connection between the Mode Model with 600 Terms and the Tangent Plane Model

In the mode model the $\cos n\theta$ and $\sin n\theta$ terms correspond to having n wavelengths around the circumference of the cylinder. Thus the wavenumber, which is the rate of change of phase with distance, is given by

$$\frac{2n\pi}{2\pi b} = \frac{n}{b} \ . \tag{3.15}$$

Cutting off the Fourier series at 600 terms corresponds to cutting off the in surface wavenumber in the shell at $600/b$.

In the tangent plane approximation this corresponds to cutting off all the transmission coefficients at values of $k > 600/b$. Now $k = k_1 \sin\phi$ so we are cutting off the transmission coefficients for $\phi > 37.7°$. Hence the Fourier series truncated at 600 terms is approximately the same as the tangent plane approximation if the value of $|T|$ dropped to 0 at $\phi \approx 37.7°$.

This suggests that the material properties of the dome deviate slightly from the values given, causing the critical angle of incidence to be reduced below 43°. However experiments to determine these material constants are not simple and it is thought that the error in the measurements may be up to 5%. The Lamé coefficients are determined by measuring the wave speed across a block of material, this gives the bulk compression speed. In order to find λ and μ separately, Young's modulus E and Poisson's ratio σ are measured statically.

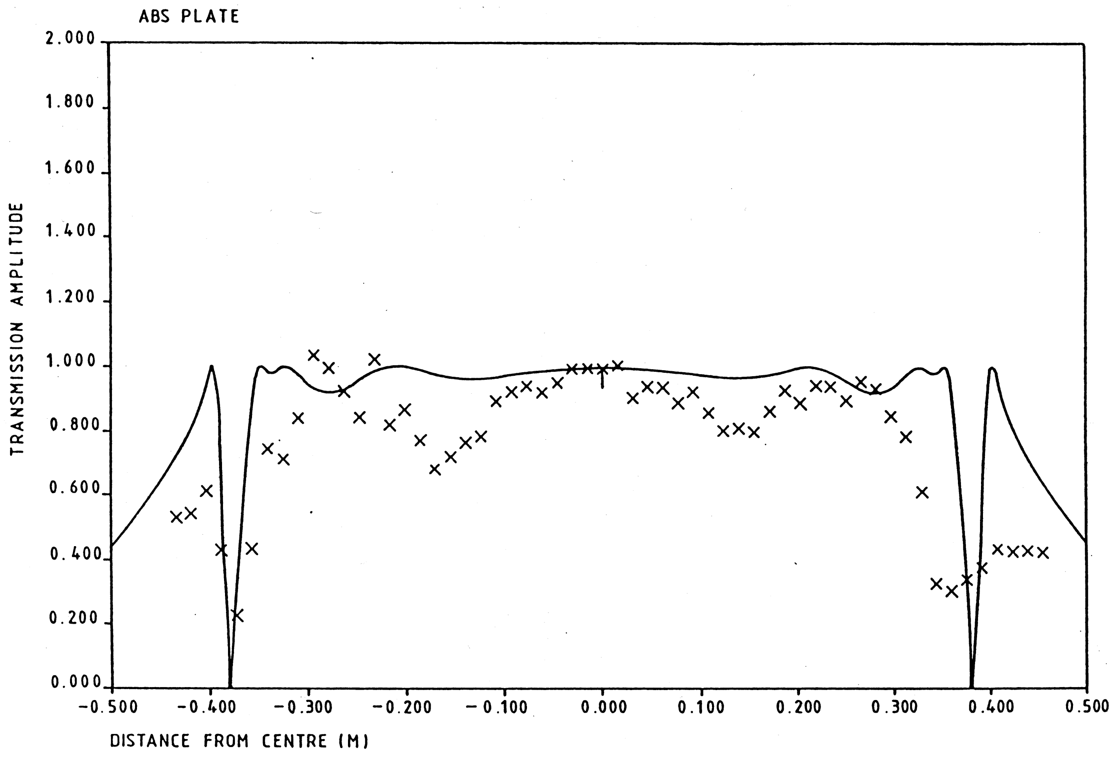

Figure 3.8: Comparison between experiment and the tangent plane method.

From the plot in figure 3.8 in which the solid curve represents the tangent plane results and the crosses represent experimental data we see that the responses towards the left agree with the tangent plane theory but further to the right responses are cut off at lower incidence. This is further evidence that either the shell material is not perfectly uniform and isotropic (perhaps due to some feature of the manufacturing process) and/or the deviations of the actual shell material from the nominal values given are such as to reduce the critical angle of incidence.

Chapter 4

Inaccuracy of the Models

There are several possible reasons for the discrepancies between the results from the two models derived in chapter 2 and the experimental data.

4.1 Equipment in the Cylinder

As well as the array of hydrophones in the cylinder there is other equipment inside the sonar set, a fact which has been ignored in both models. The form of p_3 in the mode model assumes that sound propagates perfectly inside the cylinder, however because of the equipment in there (including the array) we do not really have this happening. Depending on the material of which the equipment in the cylinder is made, it will either not allow sound waves to pass through it or sound waves passing through it will be distorted but in either case the perfect propagation assumed in the models is prevented by this equipment. Also sound waves can reflect off the solid objects and these reflected waves may hit the array directly, thus altering the response there.

4.2 Sound Passing through the Array

We stated earlier that in both models we would assume that sound passes through the array as if it were not there, whereas in fact a sound wave can only hit one point on the array before the sound is distorted so the models often count a second response which has an incorrect transmission coefficient.

4.3 Directionality of the Hydrophones

We also stated earlier that we would assume that the array hears from behind. Although the array will have some response to sound incident from behind, it will not be of the simple form we assume.

4.4 Reflections off the Walls of the Cylinder

As well as reflecting off the other equipment in the cylinder, sound waves can also reflect off the walls but in the tangent plane model we assume that when a wave enters the sonar set if it does not hit the array before it next hits the wall then it never hits the array.

4.5 End Caps of the Cylinder

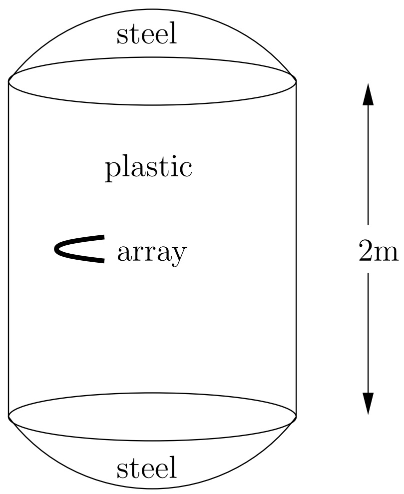

Figure 4.1: The sonar set with steel hemispherical end caps.

The sonar set is not an infinite cylinder as the models assume. In fact it is a cylinder with a vertical height of approximately 2m and although the array is not exactly at the middle of this 2m height, it is well within the middle third. The cylinder also has hemispherical steel end caps as in figure 4.1. The presence of these end caps will have two main effects:

1) The joining of the plastic and steel will scatter the elastic waves that would occur in an infinite cylinder so there needs to be an adjustment to the vibration field

in the cylinder.

2) The junction of the plastic and steel will also scatter sound waves which may reach the array directly or reflect off the cylinder walls or the other equipment to hit the array.

These effects will be discussed in more detail later.

4.6 The Ring Frequency and the Tangent Plane Approximation

We stated at the beginning of chapter 2 that the tangent plane model was only valid at high frequencies but that this should not cause a problem. We now see the reason for this by defining the ring frequency ω_R for the bending of a shell of radius a by

$$\omega_R = \frac{1}{a}\sqrt{\frac{E}{\rho}} \tag{4.1}$$

where E is Young's modulus.

It is known that generally effects due to the curvature are very important around and below ω_R but these effects are very small at frequencies much larger than ω_R. (See [6] for more details).

Our values of a, E and ρ give

$$\frac{1}{2\pi a}\sqrt{\frac{E}{\rho}} \approx 438.5Hz \tag{4.2}$$

but the frequencies we are considering are in excess of $400kHz \gg \omega_R$ so the fact that the tangent plane method neglects the curvature of the shell should be a good approximation at these frequencies.

Chapter 5

Extensions to the Models

5.1 Extensions to the Tangent Plane Model

5.1.1 Use of Blocking

We make the same assumptions as in the simplest tangent plane approximation except that, instead of assuming that the sound passes through the array as if it were not there, we use *blocking* as in figure 5.1. This is not quite what would occur in a physical situation since then there would be a response at b but not of the form we have assumed as the sound is distorted on passing through the array.

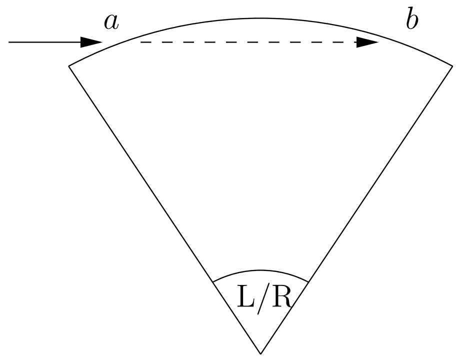

Figure 5.1: Use of blocking means only a hears the sound.

We note that since the angle at the centre of the array arc is $\frac{L}{R} = 2\alpha_0$ the use of blocking only makes a difference for waves incident from angle θ within α_0 of $\pm\frac{\pi}{2}$.

5.1.2 No Hearing from Behind

In addition to the assumption of blocking we now also assume that the array cannot hear from behind. For the array to be hit from behind, a wave must either

1) come from in front and pass through the array then hit it behind at another point in such a way as b is hit behind in figure 5.1.

2) come from behind and pass through the line $x = x_0$ with $y_n \leq y \leq y_0$ as in figure 5.2.

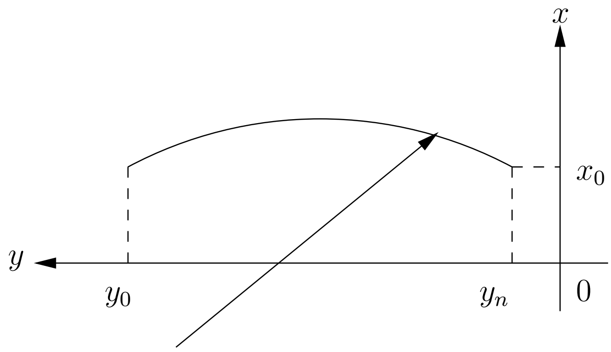

Figure 5.2: A point being hit from behind.

The first option has already been ruled out by the use of blocking so the array does not hear from behind if, when a wave from angle θ hits $\mathbf{x}_j$ having first passed through the line $x = x_0$ with $y_n \leq y \leq y_0$ then the response at $\mathbf{x}_j$ is zero. We note that this extra assumption only causes the beam pattern to change for waves from angle θ in the ranges $(-\pi, -\frac{\pi}{2})$ and $(\frac{\pi}{2}, \pi)$.

5.1.3 Reflection of Waves

Now we simply assume that

- we have a 2-D problem so the effects of the end caps cannot be accounted for
- the cylinder is filled with water so the equipment in the cylinder is ignored

so we are now allowing waves to reflect off the walls of the cylinder.

As before, let $\mathbf{x}_j$ be a point on the array which is hit by a wave from angle θ and let $\tilde{\mathbf{x}}$ be the point where this wave enters the cylinder so

$$\tilde{x} = x_j + \beta \cos\theta \tag{5.1}$$

$$\tilde{y} = y_j + \beta \sin\theta \tag{5.2}$$

$$\text{with} \quad \beta = -(x_j \cos\theta + y_j \sin\theta) + \sqrt{b^2 - (y_j \cos\theta - x_j \sin\theta)^2} \tag{5.3}$$

and the angle of incidence ϕ on the cylinder is

$$\phi \;=\; \sin^{-1}\left(\frac{y_j\cos\theta - x_j\sin\theta}{b}\right) \tag{5.4}$$

and we can calculate the response $s_{j,0}(t)$ at $\mathbf{x}_j$ as before.

Now suppose that the wave did not enter the cylinder at $\tilde{\mathbf{x}}$ but that a wave from $\hat{\mathbf{x}}$ hit the cylinder at $\tilde{\mathbf{x}}$ then the wave reflected and hit the array at $\mathbf{x}_j$. This changes the phase of the wave so we must re-evaluate it.

The Phase of the Wave

Part of the phase of the wave is given by the reflection coefficient, it is the other part we shall consider here coming from the path through the water which will contribute $e^{ik_1(L_p)}$. It is this path length, L_p, which we have to determine. We define L_p to be the sum of the distance from $\mathbf{x}_j$ to $\tilde{\mathbf{x}}$ on the inside, the distance from $\tilde{\mathbf{x}}$ on the inside to $\hat{\mathbf{x}}$ on the inside and the distance from $\hat{\mathbf{x}}$ on the inside to point d. In order to define point d consider a wave front which will first hit the cylinder at the point where it is tangential to the circle $r = a$. At this moment, the part of the wave front which will pass through the point $\hat{\mathbf{x}}$ is at point d (as in figure 5.3).

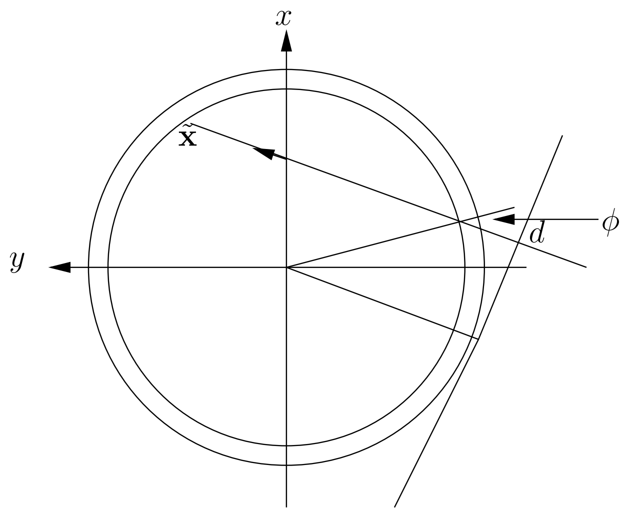

Figure 5.3: The position of point d.

Hence the response at $\mathbf{x}_j$ due to this reflected wave is

$$s_{j,1}(t) \;=\; T(\phi)R_1(\phi)p_0 e^{-i\omega t} e^{ik_1(2b\cos\phi + a + x_j\cos(\theta-2\phi) + y_j\sin(\theta-2\phi))} \tag{5.5}$$

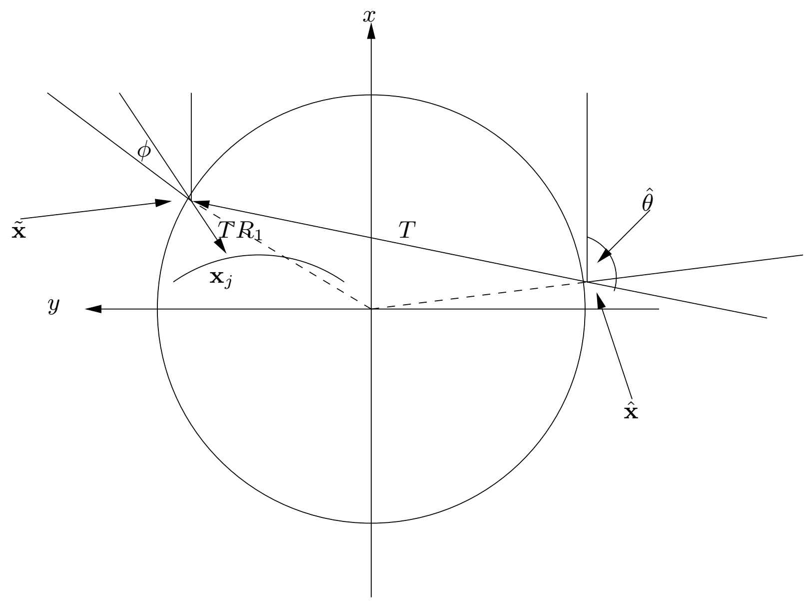

Figure 5.4: The reflection of a wave.

where $R_1 = R(\phi)e^{2ilh}$ is the amplitude ratio at the solid surface, T and R are defined by (2.75) and $\theta = -\hat{\theta}$.

The position of $\hat{\mathbf{x}}$ can be found using a little elementary geometry

$$\hat{x} = \tilde{x} - d_1 \quad \text{where } d_1 = 2\cos\phi(\tilde{x}\cos\phi - \tilde{y}\sin\phi) \tag{5.6}$$

$$\hat{y} = \tilde{y} - d_2 \quad \text{where } d_2 = 2\cos\phi(\tilde{y}\cos\phi + \tilde{x}\sin\phi) \ . \tag{5.7}$$

We can continue with more reflections although at each reflection we must check that the wave does not hit the array as otherwise the wave would not travel as far as the other side of the cylinder to reflect again.

After n reflections the response at $\mathbf{x}_j$ is

$$s_{j,n}(t) = T(\phi)\,(R_1(\phi))^n\, p_0 e^{-i\omega t} e^{ik_1(L_p)} \tag{5.8}$$

(where the L_p is the path length as defined above). Hence the array output after allowing for up to N reflections is

$$s(t) = \sum_j w_j \sum_{n=0}^{N} s_{j,n}(t - \Delta_j) \ . \tag{5.9}$$

5.1.4 Results of the Tangent Plane Model Extensions

In each of the extensions to the tangent plane approximation we plot the beam pattern by using the same equally spaced points on the array and the same set of discrete θ values as in the simplest tangent plane approximation discussed in chapters 2 and 3. We shall also restrict ourselves to the case when μ is complex.

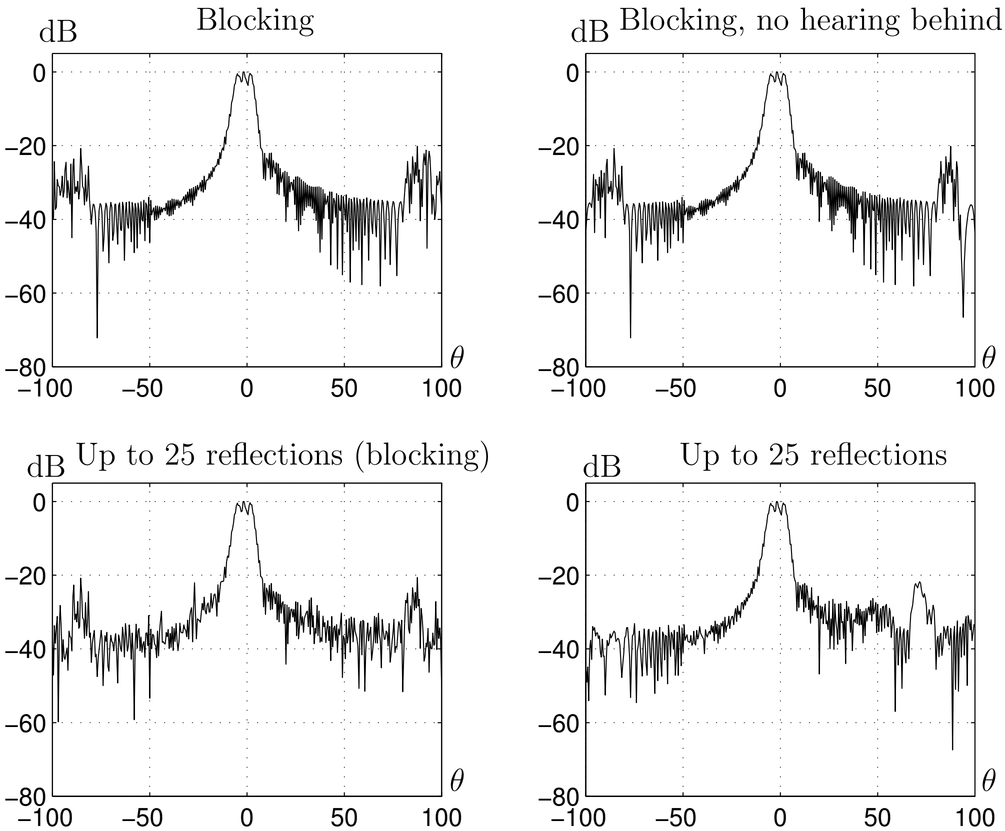

Figure 5.5: The beam patterns produced by the extensions to the tangent plane model.

Firstly we introduced blocking although in this approximation the array can still hear from behind. The majority of the beam pattern (as seen in figure 5.5 top left) is the same as in the simplest case in that we have a main lobe with beam centre -1.7° and beam width 8.7°. This main lobe is not quite symmetric and has three distinct peaks. However the depressions at $\pm 90^\circ$ (which lie inside the regions where changes are possible) have disappeared and become peaks although they are over 20dB less than the main peak. The peak at 90° consists of three distinct spikes, whilst that at -90° is oscillating even more.

Secondly we consider the case where we do not let the array hear from behind (see figure 5.5 top right). We note that the peak at 90° is now thinner than in the previous case, consisting of only two spikes and the peak centred around −90° is now slightly less oscillatory.

The third case discussed is when we allow the sound to reflect off the walls of the cylinder. Before plotting a beam pattern we have to decide a maximum number of reflections we are going to allow. We choose to have up to 25 reflections and then for $-\frac{\pi}{2} \leq \phi \leq \frac{\pi}{2}$, we have $|T||R_1(\phi)|^{25} < 0.02$.

If we now plot the beam pattern (figure 5.5 bottom left) the main lobe is again centred on −1.7° and its beam width is 8.7°. Again it has three peaks, though the troughs between the peaks seem deeper than before. There are now peaks at about ±85° but these are over 20dB down on the main lobe.

The results of using the tangent plane model in its simplest form but with up to 25 reflections off the walls of the cylinder are plotted in figure 5.5 bottom right. Again the beam centre is −1.7° and the beam width is 8.7°. The peak at 85° is still there but the peak at −85° has disappeared.

5.2 The Mode Model : An Alternative Interpretation

We now show how we can extract the wave-field travelling in certain directions from the full mode model solution.

We use a similar approach to the mode model to write the field inside the cylinder as

$$p_3 = e^{-i\omega t} p_0 \sum_{n=-\infty}^{\infty} i^n \tilde{g}_n J_n(k_3 r) e^{in\theta} \quad . \tag{5.10}$$

Using the relationship $J_{-n}(z) = (-1)^n J_n(z)$ we find that the new coefficients of interest $\tilde{g_n}$ are related to the old ones by

$$\tilde{g}_n = g_n \tag{5.11}$$

$$\tilde{g}_{-n} = g_n \tag{5.12}$$

(for $n \geq 0$), then expressing $J_n(k_3 r)$ in its integral form

$$J_n(k_3 r) = \frac{1}{2\pi i^n} \int_0^{2\pi} e^{ik_3 r \cos\phi} e^{-in\phi} d\phi \tag{5.13}$$

we can write

$$p_3 = \frac{p_0 e^{-i\omega t}}{2\pi} \int_0^{2\pi} \sum_{n=-\infty}^{\infty} \tilde{g}_n e^{ik_3 r\cos\phi} e^{-in\phi} e^{in\theta} d\theta \quad . \tag{5.14}$$

Defining $\psi = \theta - \phi$ yields

$$p_3 = \frac{p_0 e^{-i\omega t}}{2\pi} \int_{\theta-2\pi}^{\theta} \sum_{n=-\infty}^{\infty} \tilde{g}_n e^{ik_3(x\cos\psi + y\sin\psi)} e^{in\psi} d\psi \quad . \tag{5.15}$$

Since the integrand has period 2π the range of integration can be replaced by $(0, 2\pi)$ and thus we can express the field inside the cylinder as

$$p_3 = \frac{p_0 e^{-i\omega t}}{2\pi} \int_0^{2\pi} F(\psi) e^{ik_3(x\cos\psi + y\sin\psi)} d\psi \tag{5.16}$$

$$\text{where} \qquad F(\psi) = \sum_{-\infty}^{\infty} \tilde{g}_n e^{in\psi} = \sum_{0}^{\infty} \epsilon_n g_n \cos n\psi \quad . \tag{5.17}$$

This provides a representation of p_3 as a linear superposition of plane waves of amplitude proportional to $F(\psi)$ in the ψ direction. A graph of $|F(\psi)|$ is shown in figure 5.6 and from this we see that $|F(\psi)|$ is symmetric about $\psi = 0$ (which is to be expected because of the cosine dependence) and there is a large peak at $\psi = 0$. This peak represents the fact that most of the acoustic field inside the cylinder is still a plane wave travelling in the direction of the incident field. The values of F for ψ away from 0 represent the multiply-reflected field that is also present in the cylinder.

5.3 Effects of the Steel End Caps

First we consider the effects due to the plastic-steel junction scattering the elastic waves which would occur in an infinite cylinder.

The steel forming the end caps is approximately 100 times stiffer than the plastic of the cylinder so we may regard the steel as rigid. Hence instead of vibrating in a 2-D mode, the cylinder vibrates in a combination of modes with nodal lines at the top and bottom. Thus the vertical wavenumber is not 0 as we assumed but $\frac{\pi}{H}$ or $\frac{2\pi}{H}$ or ... (where H is the height of the cylinder). This effect would be worst if we have an incident wave with a vertical component giving the motion of the cylinder as described.

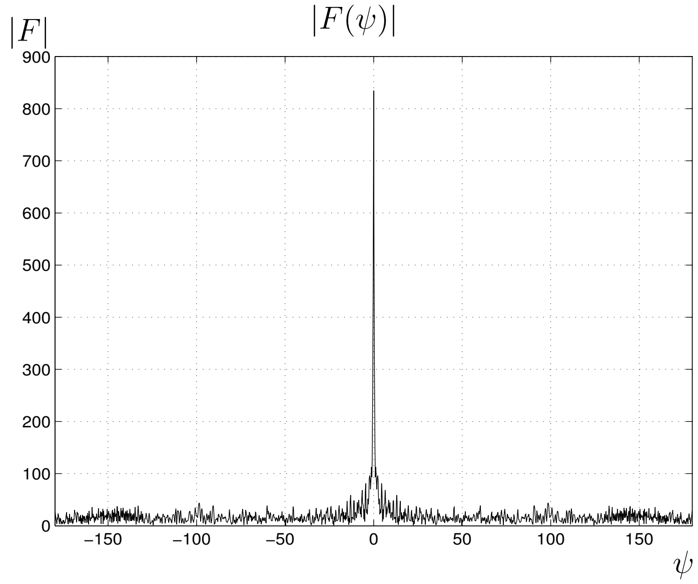

Figure 5.6: A graph of $|F(\psi)|$.

However, the acoustic wavenumber is $\frac{2\pi f}{c_1}$ which is in excess of 1675 but the vertical wavenumber is $\frac{\pi}{H} = 1.57$ which is less than 0.1% so effects are likely to be small. Higher order vertical modes may have more effect but it seems unlikely they will be excited very much.

Secondly we consider the diffraction at the plastic steel junction. The most common diffraction problem is a plane wave incident on a semi-infinite flat plate. The solution of this uses the Wiener-Hopf technique (as seen in [4] and [9]) and it can be shown that the diffraction field from the edge has amplitude proportional to $\sqrt{\frac{2}{\pi k_1 r}}$ times the incident field and some directional dependence. Here, $k_1 \geq 1675$ (the acoustic wavenumber as defined above) and r is the distance of the array from the plastic-steel junction and is about 1m when the array is in the middle of the cylinder. Hence $\sqrt{\frac{2}{\pi k_1 r}} \leq 0.019$ which is over 34dB down on the incident field, suggesting that this will not have much effect. This conclusion is unlikely to be altered significantly by the curvature of the shell, or any other complicating effects for example its thickness or further diffraction from other objects in the cylinder.

(The problem of sound scattering on a line junction of flat plates of two different materials is solved in [1]).

5.4 Two Simple Models of Equipment in the Cylinder

5.4.1 Model 1

As a simple model of some equipment in the cylinder we consider another cylinder inside the sonar set made of the same plastic material whose z-axis coincides with the z-axis of the original cylinder and whose radius is small enough not to obstruct the array. This restriction on the radius, δ, means we require $\delta \leq 0.118$. As before we can produce a formally complete solution to this problem including all the reflections off the new cylinder by using an approach identical to that of the original mode model. This time however the region 3 inside the cylinder does not contain the origin so p_3 must now contain Bessel functions of the second kind as well as the first. Hence

$$p_3 = p_0 e^{-i\omega t} \sum_{n=0}^{\infty} i^n \epsilon_n (g_n J_n(k_3 r) + h_n Y_n(k_3 r)) \cos n\theta \quad . \tag{5.18}$$

If we now express the elastic material of the inner cylinder as 4 the displacement vector in 4 can be written $\mathbf{u} = -\nabla \Psi_4 + \nabla \wedge \mathbf{A_4}$ where

$$\Psi_4 = p_0 e^{-i\omega t} \sum_{n=0}^{\infty} i^n \epsilon_n t_n J_n(k_L r) \cos n\theta \tag{5.19}$$

$$(A_4)_z = p_0 e^{-i\omega t} \sum_{n=0}^{\infty} i^n \epsilon_n s_n J_n(k_T r) \sin n\theta \tag{5.20}$$

only Bessel functions of the first kind being taken because medium 4 contains the origin and $\mathbf{u}$ must be regular there.

We now apply the usual boundary conditions at the interfaces $r = a, b, \delta$ to get a system of nine linear equations to be solved in order to find the coefficients g_n and h_n. The beam pattern can then be calculated in the same way as before.

5.4.2 Results of Model 1

Since we are considering the solid cylinder to be made of the same material as the solid forming the sonar set, the speeds of compressive and shear waves are the same in mediums 2 and 4. Taking $\delta = 0.1$ we find that the nine by nine matrix we have to solve to find g_n and h_n is almost singular for $n = 501$, hence we have taken p_3 to be a sum containing only 500 terms. As before we consider 414 equally spaced points on the array and plot the beam pattern for a discrete set of 1000 points θ between $\pm 100°$. The results of this are shown in figure 5.7 (left).

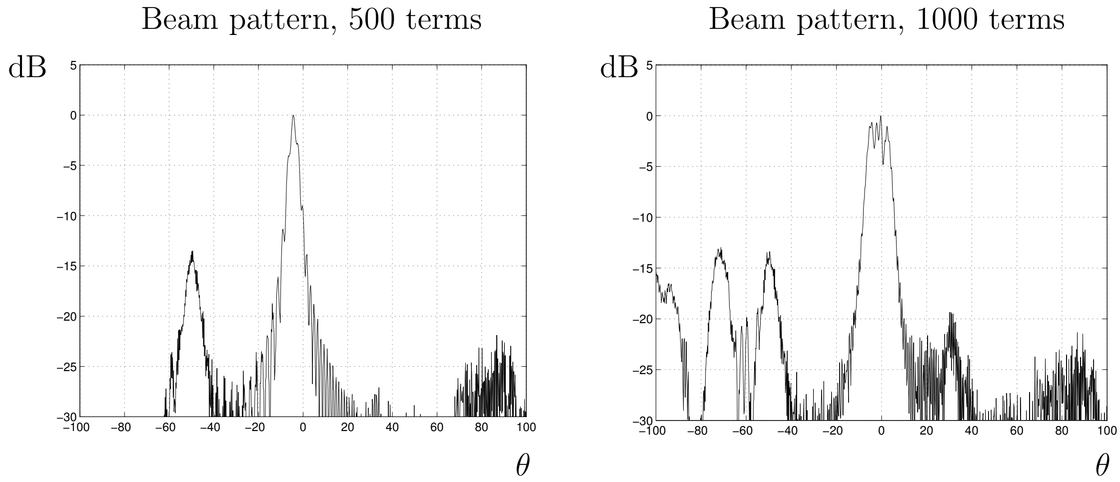

Figure 5.7: The beam patterns produced with an elastic cylinder in the sonar set.

It is immediately noticeable that the beam is centred well to the left of $0°$, in fact the beam centre is $-4.4°$. The beam is also considerably narrower than before, the beam width being only $5.198°$. The main lobe is now a single peak instead of having several peaks and depressions as occurred in the case when there was no cylinder present inside the sonar set. There is still a side lobe at about $-50°$ which is about 14dB down on the main lobe.

On examining the values of g_n and h_n more closely for this problem it is found that for n beyond about 200, $h_n = 0$ and g_n is equal to the scattering coefficients for the original problem. Hence for large n we can use the original six by six matrix to calculate g_n. This produces the graph in figure 5.7 (right) which has a beam width of $10.75°$ and a beam centre at $-1°$. The beam pattern has a very similar form to that produced by the original mode model in that the main lobe has four spikes and there are side lobes at $-50°$, $-70°$ and $-100°$.

5.4.3 Model 2

Again we consider a cylinder inside the sonar set whose z-axis coincides with the z-axis of the original cylinder but this time we assume that the object is rigid. As before we use the same approach as the mode model and p_3 must contain Bessel functions of the first and second kind. However since the inner cylinder is now rigid there is no displacement in medium 4 so we only have seven unknowns. The seventh boundary condition to be used to determine these unknowns is that $u_r = 0$ at $r = \delta$, ie

$$\frac{1}{\rho_3\omega^2}\frac{\partial p_3}{\partial r} = 0 \qquad \text{at } r = \delta \ . \tag{5.21}$$

Thus the coefficients extra to those in the six by six matrix are

$$\alpha_{47} = -\left(\frac{y_3}{k_3}\right)^2 Y_n(y_3) \tag{5.22}$$

$$\alpha_{57} = -y_3 Y_n'(y_3) \tag{5.23}$$

$$\alpha_{76} = J_n'(z_3) \tag{5.24}$$

$$\alpha_{77} = Y_n'(z_3) \tag{5.25}$$

where $z_3 = \delta k_3$.

5.4.4 Results of Model 2

We use the same parameters as in the first model but this time p_3 is a sum of only 400 terms since this time the matrix is almost singular for $n = 410$. The result of this is to produce a beam pattern in which the main beam has a width of 4.625° and the beam centre is −6.2° (as in figure 5.8 top left). Again there is a side lobe at −50° which is about 12dB down on the main lobe but this time there is only one peak. However, on plotting $|g_n|$ and $|h_n|$ for n up to 400, (figure 5.8 top right and bottom left) we see that for $n \geq 154$ we have $h_n = 0$, hence for $n \geq 400$ we can take $h_n = 0$ and then we simply have to solve the six by six matrix as in the mode model described in chapter 2. The results of this are shown in figure 5.8 bottom right and can be seen to be very similar to those produced by the original mode model. The beam width is now 10.71°, the beam centre is −1.2° and again the main lobe has four distinct peaks. Side lobes centred on −50° and −70° of about 13dB down on the main lobe are present and there is also a side lobe at −100° of about 15dB down on the main lobe. It is hardly surprising that these results are so similar to the mode model since it is only for $n < 154$ that the terms in the sum are any different. If we make δ smaller h_n is zero for a smaller value of n so the sum becomes even more like the original mode model. We should expect h_n to be small since $Y_n(\delta) \to \infty$ as $n \to \infty$ for small δ so we do not want these terms to dominate the sum.

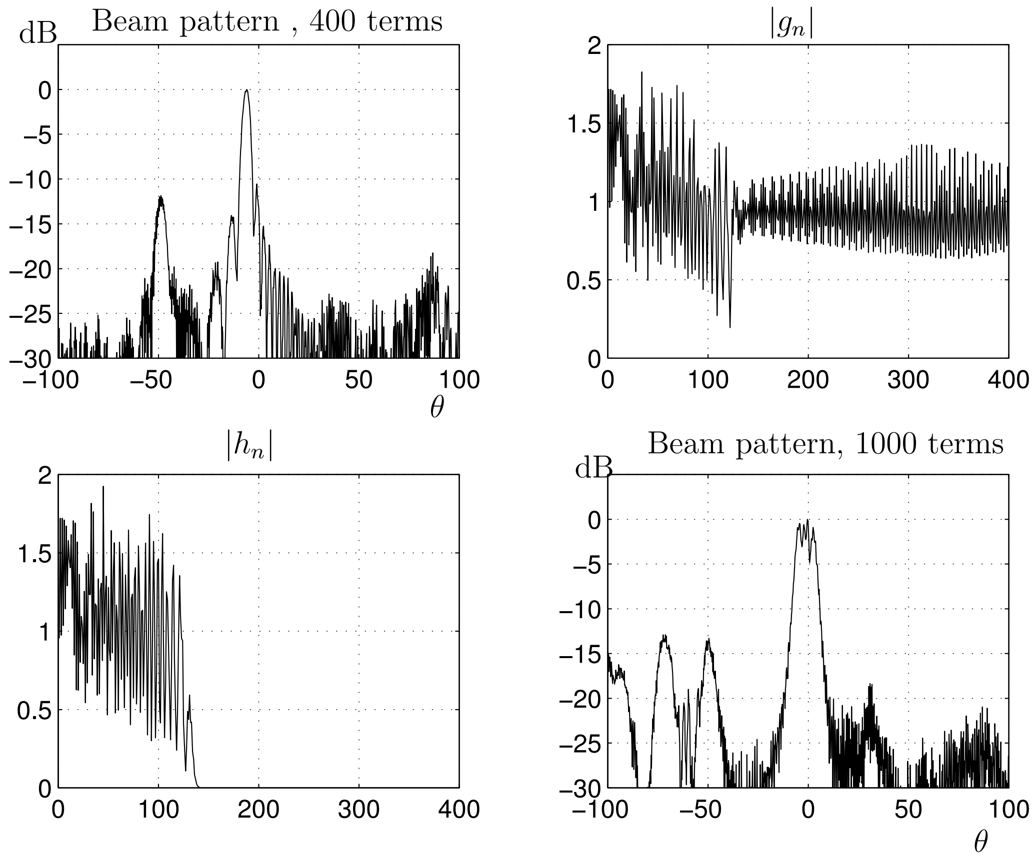

Figure 5.8: The beam pattern produced with a rigid cylinder inside the sonar set.

An alternative explanation as to why it is valid to calculate g_n using the original six by six matrix for large n is that we can eliminate the seventh line in the seven by seven matrix by writing

$$h_n = -\frac{\alpha_{76}}{\alpha_{77}} g_n \tag{5.26}$$

where α_{76} and α_{77} are given by (5.24) and (5.25). We then have to solve a six by six system in which the entries are the same as for the original mode model except

$$\alpha_{46} = -\left(\frac{y_3}{k_3}\right)^2 \left(J_n(y_3) - Y_n(y_3)\frac{J_n'(z_3)}{Y_n'(z_3)}\right) \tag{5.27}$$

$$\alpha_{56} = -y_3 \left(J_n'(y_3) - Y_n'(y_3)\frac{J_n'(z_3)}{Y_n'(z_3)}\right) \quad . \tag{5.28}$$

Now $z_3 \approx 188$ for $\delta = 0.1$ so we would expect the ratio $J_n'(z_3)/Y_n'(z_3)$ to matter for n up to 188 but for n beyond this it will quickly get much smaller. Thus we would expect the coefficients g_n for this problem to be very close to the coefficients for the original problem for n beyond about 188 and hence we can use the original six by six matrix.

Chapter 6

Conclusions

We have studied several mathematical models of the sonar set and compared the results they produced with experimental findings. Both the mode model and the tangent plane approximation produced the correct form of asymmetry of the main beam although the agreement produced by the mode model was closer when there were only 600 terms in the sum rather than 1000. This cut off at 600 terms has been seen to correspond to the tangent plane model if the absolute value of the transmission coefficients dropped to zero at $\phi \approx 37.7°$. The actual cut off using the experimentally observed values of E and σ is $\phi = 43.3°$, suggesting a significant deviation of these material constants from the values used. The asymmetry produced by the tangent plane method has been explained using the method of stationary phase, this explanation suggests that if $|T|$ dropped to zero for a smaller critical angle of ϕ then the beam would be narrower and the beam centre would be further to the left. This result corresponds to the fact that the 600 term mode model has a narrower main beam, centred further to the left than the main beam produced by the 1000 term model.

We have seen that the array is positioned in an area in which the beam width is varying rapidly and that this rapid variation is due to the near critical incidence on the shell. Hence the beam width is also sensitively dependent on the value of this critical angle and when designing such an array as this, it should be checked that

1) the rays contributing to the main term in the stationary phase approximation are not so oblique to the shell that they are reduced in amplitude by effects of the critical angle

2) this criterion should remain true even if the material properties deviate from the nominal values somewhat, in a way that reduces the critical angle.

Further evidence that the shell material is not perfectly uniform and isotropic or that the material constants differ slightly from the values stated was given by the graph comparing the tangent plane method and experimental data (see figure 3.8) in which the experimental responses are cut off before those of the tangent plane method.

Neither the original tangent plane approximation nor its extensions seem to reproduce the side lobe at 100° although the model incorporating up to 25 reflections produces a side lobe at 70° and, in agreement with experimental evidence, there are no peaks for negative θ. It seems that of all the tangent plane approximations this one models the physical situation the best, in that the beam pattern it produces resembles the experimentally observed beam pattern the most closely. This suggests that reflections are considerably more important than the changes in transmission coefficient due to a wave passing through the main transmitting array or the straight receiving array below it. We also saw, by defining the ring frequency ω_R, that neglecting curvature is a valid approximation at the high frequencies we are considering. The mode model produces more side lobes than the tangent plane method, however they are mostly centred on negative values of θ.

The steel end caps on the cylinder would seem to have little significant effect, the plastic steel junction scattering the elastic waves which would occur in an infinite cylinder produces a vertical wavenumber which is about 0.1% of the acoustic wavenumber and the diffraction at the plastic steel junction only produces an amplitude 34dB down on the incident field.

It is difficult to model the effects caused by the equipment inside the cylinder however we have studied a coaxial cylindrical obstruction which can be treated by a simple extension to the mode model. The results produced are not noticeably much different from those produced by the original mode model, the similarity being more noticeable the smaller the radius of the cylindrical object. However this form of model for equipment is probably far too simple and more work is needed on this problem.

The main conclusion is that the positioning of the array makes its response extremely sensitive to the critical angle of incidence for the shell. Thus if the material properties of the dome deviate even slightly from the values given, the response changes which could account for the discrepancies between theory and experiment.

Appendix A

Numerical Values of Physical Parameters

The numerical values of the physical parameters used are given by

density of sea water	ρ_1	1030kg/m^3
speed of sound in water	c_1	1500m/s
density of solid layer	ρ_2	1050kg/m^3
Lamé coefficients	λ	3.39 x 10^9N/m^2
	Re(μ)	7.82 x 10^8N/m^2
	Im(μ)	-0.02 x Re(μ)
Young's modulus	E	2.2 x 10^9N/m^2
Poisson's ratio	σ	0.4063
frequency of waves detected	f	VHF (in excess of 400kHz)
inner radius of cylinder	b	0.5205m
outer radius of cylinder	a	0.53m
height of cylinder	H	2m
centre of array	x_c	0.141m
	y_c	0.2685m
radius of array	R	0.865m
length of array	L	0.2295m

(Note that the length L of the array is chosen to allow 18 array elements with centre to centre spacing of 12.75mm).

References

[1] P.R. Brazier-Smith. Scattering by fluid-loaded co-planar half-plane plates. *Elastic Wave Propagation* 247-251, 1989

[2] R.D. Doolittle and H. Überall. Sound Scattering by Elastic Cylindrical Shells. *JASA*, **39**:272-275, 1966

[3] J.J. Faran Jr. Sound Scattering by Solid Cylinders and Spheres. *JASA*, **23**:405-418, 1951

[4] D.S. Jones. Acoustic and Electromagnetic Waves. Clarendon Press, 1986 (chapter 9)

[5] L.D. Landau and E.M. Lifschitz. The Theory of Elasticity. Pergamon Press Ltd, 1970

[6] A.W. Leissa. Vibration of Shells. *NASA SP-288*, 1973

[7] J. Lighthill. Waves in Fluids. Cambridge University Press, 1986

[8] W. Madigosky and R. Fiorito. Modal Resonance Analysis of Acoustic Transmission and Reflection Losses in Viscoelastic Plates. *JASA*, **65**:1105-1115, 1979

[9] P.M. Morse and K.U. Ingard. Theoretical Acoustics. Princeton University Press, 1986

[10] J. Urick. Principles of Underwater Sound. McGraw-Hill Book Company, 1975